CHARACTERIZATION OF A HALL EFFECT THRUSTER USING THERMAL IMAGING

THESIS

James William Tomaszewski, Captain, USAF

AFIT/GA/ENY/07-M18

DEPARTMENT OF THE AIR FORCE
AIR UNIVERSITY

AIR FORCE INSTITUTE OF TECHNOLOGY

Wright-Patterson Air Force Base, Ohio

APPROVED FOR PUBLIC RELEASE; DISTRIBUTION UNLIMITED

The views expressed in this thesis are those of the author and do not reflect the official policy or position of the United States Air Force, Department of Defense, or the U.S. Government.

AFIT/GA/ENY/07-M18

CHARACTERIZATION OF A HALL EFFECT THRUSTER USING THERMAL IMAGING

THESIS

Presented to the Faculty

Department of Aeronautics and Astronautics

Graduate School of Engineering and Management

Air Force Institute of Technology

Air University

Air Education and Training Command

In Partial Fulfillment of the Requirements for the

Degree of Master of Science in Astronautical Engineering

James William Tomaszewski, BSME

Captain, USAF

March 2007

APPROVED FOR PUBLIC RELEASE; DISTRIBUTION UNLIMITED

AFIT/GA/ENY/07-M18

CHARACTERIZATION OF A HALL EFFECT THRUSTER USING THERMAL IMAGING

James William Tomaszewski, BSME

Captain, USAF

Approved:

Richard D. Branam, Maj, USAF (Chairman)	6 Mar 07 Date
Lt Col Raymond C. Maple, USAF (Member)	14 Mar 07 Date
Dr. William Hargus (Member)	3-8-07 Date

AFIT/GA/ENY/07-M18

Abstract

A Hall thruster uses ionized xenon as a propellant for space propulsion applications. The heat produced by thruster components and the xenon plasma transfers to space and the spacecraft, impacting thruster and spacecraft design, as well as thruster efficiency and lifetime. Therefore, thermal information was gathered and analyzed in order to better understand the thermal characteristics of an operating thruster and to provide data applicable to improving the thruster efficiency and lifetime.

This paper contains analysis of thruster temperatures obtained using a commercially available FLIR A40M thermographic imager in order to characterize a Busek Inc. 200W Hall Effect Thruster operating in Chamber 6 at the Air Force Research Laboratory at Edwards AFB, CA. This method is non-intrusive in that the thruster is viewed from outside the chamber through a zinc selenide window and provides temperature data on the entire visible area of the thruster for output to a computer for further processing. Maximum temperatures observed were above 773 K on the alumina plasma sprayed portion of the cathode, the anode, and on the thruster body near the exit plane. Magnet core winding temperature varied from 620 K near the exit plane to 475 K near the rear of the thruster. If these temperatures are near the magnet core temperature, it suggests they are not near the Curie temperature for iron of 1043 K or the Curie temperature of 858 K of iron alloyed with nickel. Initial heating rates of up to 138 K/min and initial cooling rates of up to 218 K/min were observed. The steady state temperature images and the heating data indicated a possible interaction between xenon and the thruster components.

Acknowledgments

The Air Force Institute of Technology would like to thank Michael Huggins at the Air Force Space Propulsion Lab for providing funding for this work. Thanks also to the Air Force Space Propulsion Lab at Edwards Air Force Base for material, financial, and personnel support in completing this project.

Capt. James W. Tomaszewski would like to thank Dr. William Hargus for sponsoring this work, and for providing a multitude of pertinent reference data. Thanks also to Taylor Matlock for his extensive help in getting this project started and for operating the thruster, and to Garrett Reed and Lt. Jared Eckholm for setting up the experiment and operating the vacuum chamber. Thank you Major Richard Branam for providing guidance as my thesis advisor. Finally, I would like to thank my parents for everything they have done for me throughout my life, and I hope I have made you proud.

Table of Contents

.....Page

Abstract iv

Acknowledgments v

Table of Contents vi

List of Tables ix

List of Figures x

I. Introduction..... 1

II. Background 5

Hall Thruster Operation and Specifications 5

Magnet temperature affects thruster efficiency and lifetime 7

Temperature affects cathode lifetime 8

Temperature affects anode lifetime 9

Thermal Imaging Option 10

Radiation and Thermal Imaging Basics.....11

Thermal Imager Used 15

Thermal imagers also used in industry 17

Error Analysis Approach 18

III. Methodology 20

Chapter Overview.....20

Hall thruster 20

Vacuum Chamber 23

Thermal Imaging Camera 24

.....Page

Window 24

Camera Software.....25

Overall Lab Setup 26

Data Collection 29

Data Analysis.....30

Thruster side view heat up, steady state, and cool down.....30

Thruster exit plane view temperatures and cool down 32

Uncertainty Analysis.....36

IV. Results and Discussion 41

Chapter Overview.....41

Heating rate results taken from thruster side view images 42

Steady state results taken from thruster side view image 47

Cooling rate results taken from thruster side view images.....50

Temperature results with exit plane facing camera 53

Cooling rate results taken from images with thruster exit plane facing camera.....57

V. Conclusions and Recommendations 62

Conclusions.....62

Recommendations for Future Research.....64

Appendix A – Data Collection Experimental Log..... 66

Thruster start up to 8.5 sccm followed by shut down and 5 hour cool down.....66

Thruster start-up to 8.5 sccm, 90° rotation, and cool down.....66

Thruster startup to 7.0 sccm and steady state 67

.....Page

Thruster flow increase from 7.0 sccm to 10.0 sccm.....68

Thruster rotation and shutdown.....68

Thruster cool-down with exit plane facing camera 68

Appendix B – Tabular Data Used for Error Analysis..... 69

Bibliography 72

List of Tables

Page

Table 1: Electric Propulsion Specific Impulse Comparison 3

Table 2: Busek Co. Inc Hall Thrusters Specifications 7

Table 3: Thermal Imaging camera comparison 16

Table 4: Values of Emissivity for selected types of steel 23

Table 5: Data Collection Summary..... 30

Table 6: Object Parameter settings in ThermaCam Researcher 32

Table 7: Object Parameter settings in ThermaCam Researcher for Anode 33

Table 8: Object Parameter Settings in ThermaCam Researcher for Exit Plane Facing Camera 33

Table 9: Object Parameter settings in ThermaCam Researcher for Cool Down with Exit Plane Facing Camera 35

Table 10: Lowest and Highest Input Values 39

Table 11: Maximum Temperature Error Using Combined Input Values 40

Table 12: Maximum Combined Temperature Error Using Simple Summation..... 40

Table 13: Steel Temperature Error Due to Emissivity..... 69

Table 14: Boron Nitride Temperature Error Due to Emissivity 69

Table 15: Alumina Plasma Spray Temperature Error Due to Emissivity 70

Table 16: Air Transmissivity Temperature Error 70

Table 17: Window Transmissivity Temperature Error 70

Table 18: Distance Temperature Error..... 71

Table 19: Reflected Temperature and Temperature Error 71

List of Figures

Page

Figure 1: Hall Thruster on SMART-1 (1) 1

Figure 2: Propulsion technology comparison (2:446) 2

Figure 3: Electric propulsion performance comparison 3

Figure 4: Hall thruster schematic (1) 5

Figure 5: Hall Thruster Firing in Vacuum Chamber 6

Figure 6: 200 Watt Hall thruster rear view (left), side view with exit plane facing right (middle), and exit plane view (right). 7

Figure 7: Magnetization vs. Temperature (7) 8

Figure 8: Hollow cathode operation. (10) 9

Figure 9: Basic radiation schematic 13

Figure 10: Schematic of thermographic imager measurement (20:183) 14

Figure 11: FLIR, Inc, ThermoVision A40M (20) 17

Figure 12: Plugged cooling fins in a heat exchanger (23). 18

Figure 13: Power plant component (left) and thermal image (right) showing fault in Ar2 (24:3) 18

Figure 14: Busek BHT-200-X3 Hall Thruster (5) 20

Figure 15: Exit plane and anode chamber discoloration 21

Figure 16: Thruster discoloration. 22

Figure 17: Schematic top down view of vacuum chamber setup 24

Figure 18: Zinc Selenide Window During Thruster Operation 25

Figure 19: Chamber and Test Setup 27

Figure 20: Thruster and yellow thermocouple wires inside Chamber 6. 28

Figure 21: Spot temperature locations on thruster 31

Figure 22: Spot Locations for Cool Down Data with Exit Plane Facing the Camera 35

Figure 23: 200W Thruster and Researcher raw thermal image. (1. Kapton tape covering thermocouple #5. 2. Magnet core. 3. Steel portion of Cathode. 4. Anode cone. 5. Reflection from rear stand on thruster mount plate. 6. Power wire for anode. 7. Axial support bars 8. Alumina plasma sprayed portion of the Cathode.) 41

Figure 24: Axial Support Heating Rate 42

Figure 25: Anode Cone Heating Rate 43

Figure 26: Steel Portion of Cathode Heating Rate 44

Figure 27: Alumina Plasma Sprayed Portion of the Cathode Heating Rate 45

Figure 28: Component heating rates in single chart 46

Figure 29: Side View Steady State Temperature Image 48

Figure 30: Emissivity and angle of emission (14:119) 49

Figure 31: Axial Support Bar Cooling Rate 50

Figure 32: Anode Cone Cooling Rate 51

Figure 33: Steel Portion of the Cathode Cooling Rate 52

Figure 34: Alumina Plasma Sprayed Portion of the Cathode Cooling Rate 53

Figure 35: ThermaCam Researcher Image of Thruster at 45° Angle to Camera 54

Figure 36: Temperature Pattern on Upper Steel Portion of the Cathode 55

Figure 37: Surface Plot of Temperatures with Exit Plane Facing Camera 56

Figure 38: ThermaCam Researcher Image of Exit Plane of Thruster Facing Camera 57

Figure 39: Exit Plane Anode Cone Cooling Rate 58

Figure 40: Rear Anode Channel Cooling Rate 59

Figure 41: Alumina Plasma Sprayed Portion of Exit Plane Cooling Rate 60

Figure 42: Cathode Tip Cooling Rate 61

CHARACTERIZATION OF A HALL EFFECT THRUSTER USING THERMAL IMAGING

I. Introduction

The objective of this work was to use a commercially available thermal imager to gather thermal information on an operating space propulsion engine in order to provide designers with data applicable to improving engine efficiency and lifetime. While many different means of space propulsion are available, studying and use of the electromagnetic Hall thruster is of current interest to the United States Air Force (USAF) and other agencies. For example, a Hall thruster will undergo testing on the USAF Space Vehicles Directorate TacSat-2, launched December 16, 2006. The Japanese/Korean MBSAT, launched in June 2004, used a Hall thruster for North-South station keeping, and the European Space Agency SMART-1 satellite shown in Figure 1 (1), launched in 2003, also used a Hall thruster (1).

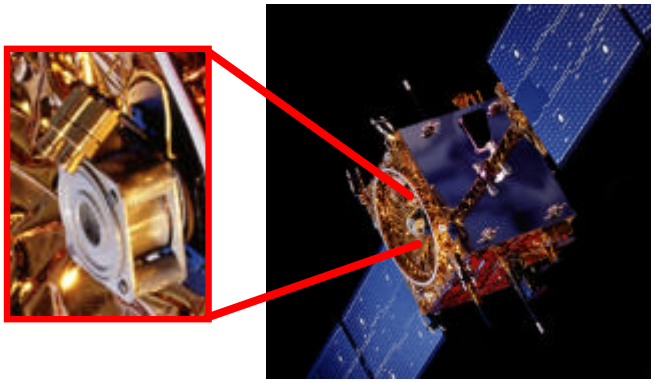

Figure 1: Hall Thruster on SMART-1 (1)

The increasing interest and use of Hall thrusters stems from their performance characteristics. Figure 2 (2:446) shows different propulsion technologies and their relation according to specific impulse and specific mass.

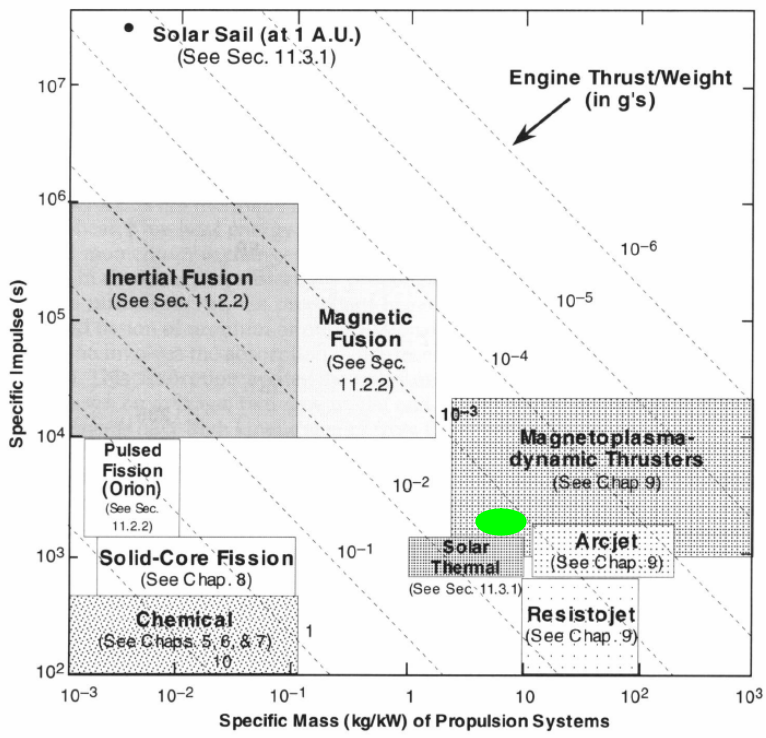

Figure 2: Propulsion technology comparison (2:446)

The area highlighted in green represents the Hall thruster technology with a specific impulse of 1600 to 2000 seconds and a specific mass of just under 10 kg/kW. The specific impulse represents the efficiency of the thruster used by the spacecraft, which impacts the overall operational capability. The Hall thruster is up to 5 times more efficient than chemical energy based thrusters using liquid propellant. The benefit of a highly efficient thruster can be a longer operational lifetime, a larger payload, or a lower launch weight, which has the benefit of lowering launch cost. Table 1 shows the specific impulse of several electric propulsion thrusters, and reveals the Hall thruster as a high performance option (3:702-708).

Table 1: Electric Propulsion Specific Impulse Comparison

	Specific Impulse (sec)
Resistojet	~ 300
Arcjet	480 - 800
Pulsed Plasma Thruster	850 – 1200
Hall Effect Thruster	1600 - 2000
Ion Thruster	2500 - 3400

With a specific impulse of 1600 seconds to 2000 seconds, these thrusters are not as efficient as ion thrusters, but they have a lower specific mass and a higher thrust to power ratio, as shown in Figure 3 with the Hall thrusters circled in green.

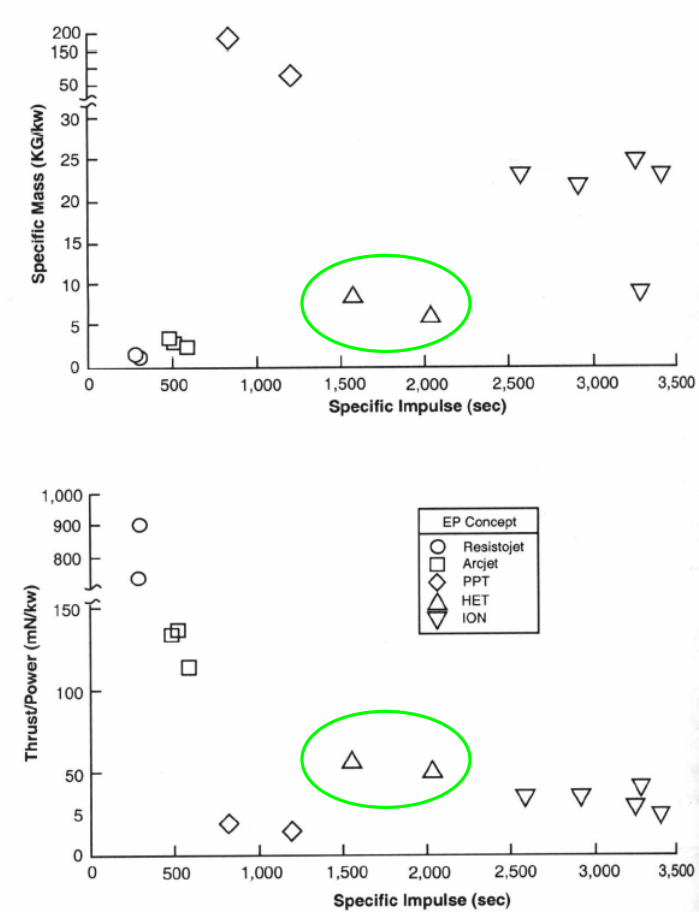

Figure 3: Electric propulsion performance comparison

Hall thrusters experience lifetime limitations above a specific impulse of 2500 (3:707). Different thruster performance characteristics taken as a whole indicate that no one thruster is "the best", rather they are suited to a particular type of mission. The capabilities of the Hall thruster best fit missions such as satellite station keeping or orbit apogee burn.

Since these thrusters operate in the harsh environment of space, ground based study is restricted to facilities that have the capability to simulate the space environment as closely as possible, such as the vacuum chambers at the Air Force Space Propulsion Lab at Edwards Air Force Base in California. Valuable research conducted at the Air Force Space Propulsion Lab contributed to improved understanding concerning the operation of electric propulsion devices, and work on individual components at other facilities exists. Therefore, if data collected on the same types of thrusters currently in use is applied to improve thruster efficiency and lifetime, future missions will benefit. In summary, the thermal information gathered and analyzed in this report will provide thruster designers with data applicable to improving engine efficiency and lifetime, which will in turn provide better thrusters for use on USAF satellites.

II. Background

This section begins with a description of how a Hall thruster operates and how temperature plays a role in thruster efficiency and lifetime. Next is a discussion of why thermal imaging was used and how thermal imaging works. This will include a discussion on radiation and the various factors affecting the temperatures output by the imager. While prior experimentation using a thermal imager to gather temperature data on an operating Hall thruster is not readily available, many applications find thermal imagers very useful and some examples will be reviewed. Lastly, the approach taken to account for theoretical and experimental errors is covered.

Hall Thruster Operation and Specifications

While a more detailed explanation of Hall thruster operation is available (4:Ch 2), basic thruster operation involves an electric and magnetic field with ionized xenon particles acting as the propellant to develop thrust, T, as shown in Figure 4.

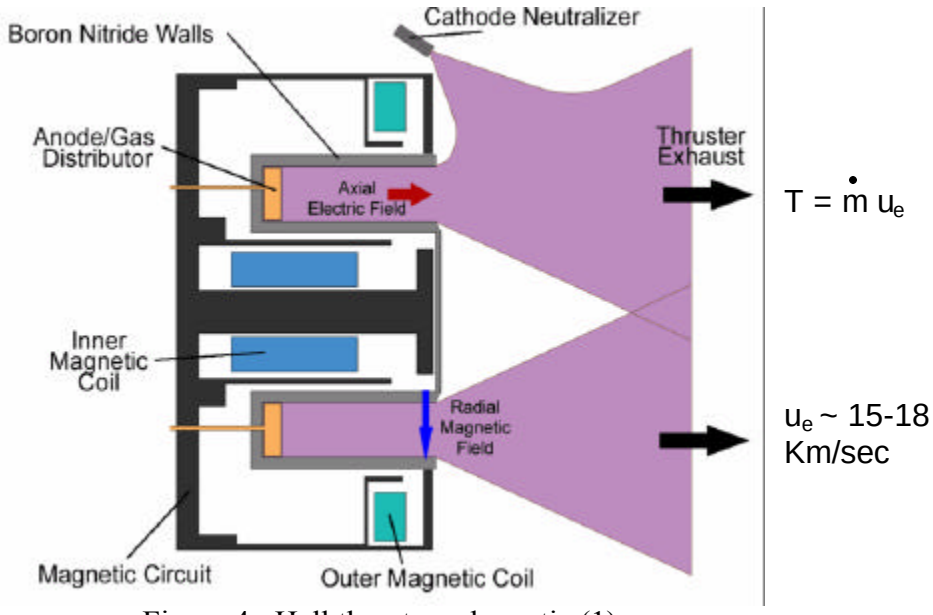

Figure 4: Hall thruster schematic (1)

The cathode uses thermionic emission of electrons from a low work function material in order to produce an electric field between the cathode and the anode. A radial magnetic field captures most of the electrons in order to keep them from being accelerated and forms a ring current (Hall current) near the exit plane of the thruster. Some of the electrons produced by the cathode do not become a part of the Hall current, rather they act to neutralize the xenon as it exits the thruster. The xenon gas injects from within the anode and electrons diffusing slowly from the Hall current to the anode ionize the xenon. The now positively charged xenon accelerates due to the force from the electric field to about 15 km/sec. As the xenon ions exit the thruster, they recombine with electrons primarily when they hit the anode channel wall to form a neutral gas. Figure 5 shows the exit plume of the Hall thruster while operating during this experiment.

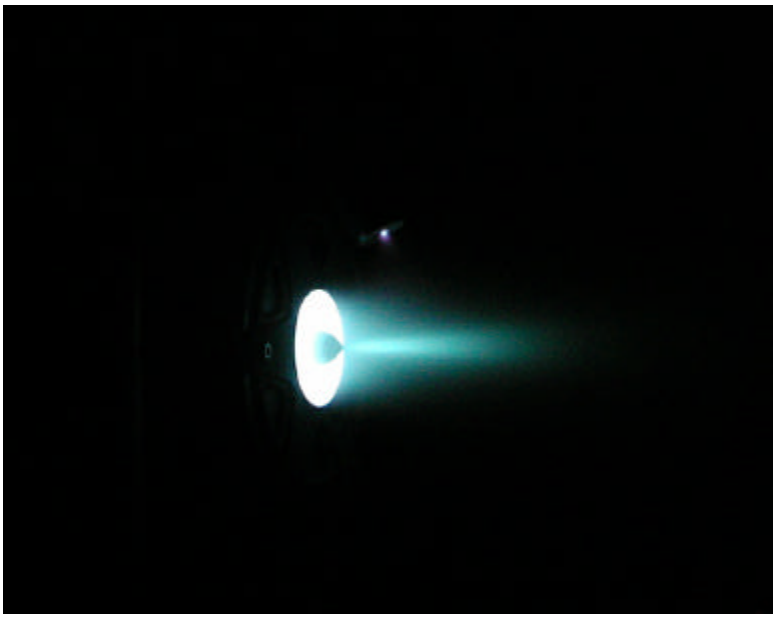

Figure 5: Hall Thruster Firing in Vacuum Chamber

The small point of light above the plume is the cathode tip, with the anode cone near the center of the image. Hall thrusters using this technology are available over a wide range of specifications (5,6), including those listed in Table 2.

Table 2: Busek Co. Inc Hall Thrusters Specifications

	BHT-200	BHT-600	BHT-1000	BHT-1500	BHT-8000	BHT-20000
Discharge Input Power (W)	200	600	1000	1700	8000	20250
Propellant Mass Flow Rate (mg/sec)	0.94	2.6	3.4	5.6	27.4	40
Thrust (mN)	12.8	39.1	58.5	102	512	1080
Specific Impulse (sec)	1390	1530	1750	1820	1900	2750
Propulsive Efficiency (%)	43.5	49.0	50.3	54.6	60.0	72.0

Figure 6 shows an image of the actual thruster used for the experiment with a rear view, side view, and exit plane view.

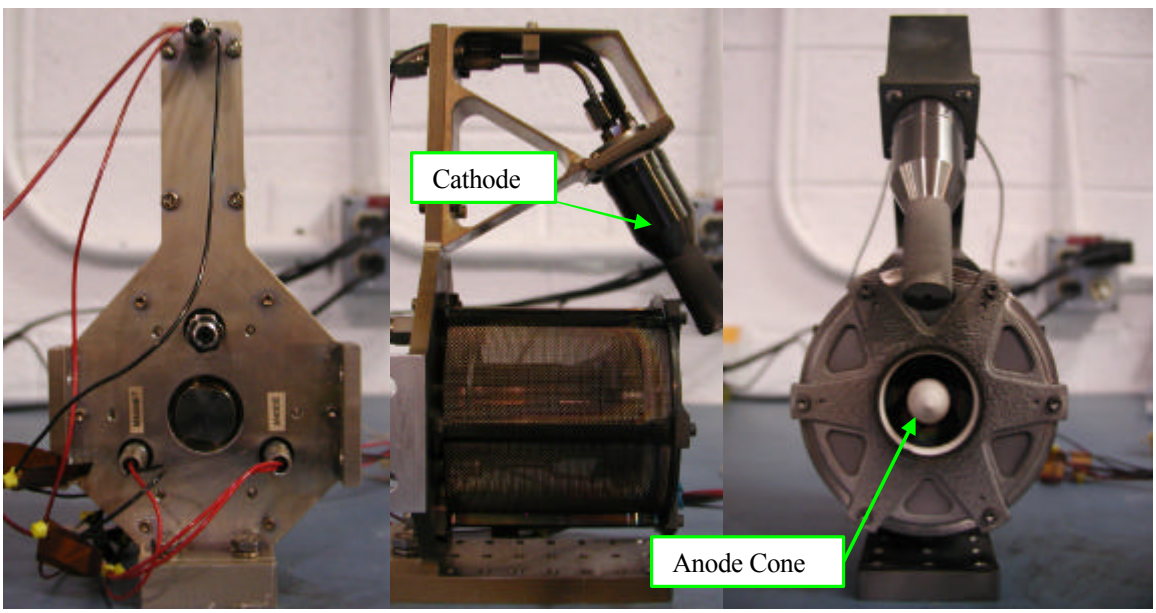

Figure 6: 200 Watt Hall thruster rear view (left), side view with exit plane facing right (middle), and exit plane view (right).

Magnet temperature affects thruster efficiency and lifetime

As discussed earlier, Hall thrusters require a magnetic field to operate, and one of the factors effecting magnetic field strength is temperature. As the temperature of a magnet increases, the magnetization of the material goes down as shown in Figure 7 (7) for Iron loaded with various amounts of silicate.

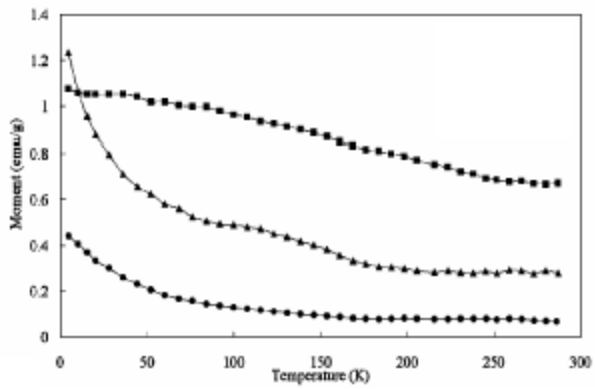

Figure 7: Magnetization vs. Temperature (7)

If the material reaches the Curie temperature, the magnetization becomes zero (8). The magnetic circuit is usually iron, sometimes alloyed with cobalt or nickel (4). Iron, for example, has a Curie temperature of 1043 K. An increase in magnet temperature and the resulting decrease in the magnetic field strength would lead to a decrease in thruster efficiency, while a loss of the magnetic field would cause the thruster to fail. This type of failure could be caused by erosion of the insulator walls and plasma shunting through the magnetic circuit (4). Accordingly, magnet operating temperature should be kept low, and well below the Curie temperature for the magnet material.

Temperature affects cathode lifetime

Knowledge of the cathode temperature is important because it impacts cathode lifetime. Hollow cathodes employ a process known as thermionic emission. In thermionic emission, a metal such as barium or a ceramic such as lanthanum hexaboride heats in order to allow the electrons' vibrational energy to overcome the electrostatic forces holding the electrons to the surface (9). The material has a low work function, which refers to the minimum energy needed to remove an electron from the material surface. About 10% or less of the propellant used by the Hall thruster passes through the

cathode (see Figure 8) and ionized by the electrons produced by thermionic emission in order for the cathode to perform its function.

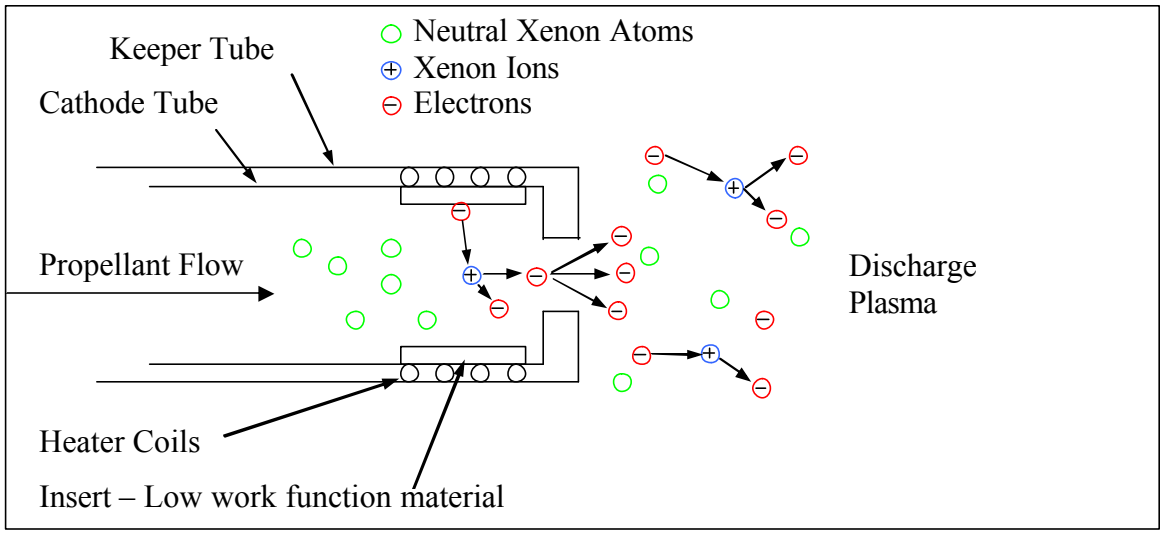

Figure 8: Hollow cathode operation. (10)

The material undergoing thermionic emission in hollow cathodes is the insert, which is most commonly barium oxide. If the insert does not function correctly, the cathode, and therefore the thruster cannot function. Since insert lifetime is temperature dependent (11:4, 12), gathering temperature data on the cathode is important.

Temperature affects anode lifetime

Anode channel wall temperatures are increased by interaction with the xenon ions in the channel. This increase in temperature may be due to radiation and ions impacting the channel wall. Therefore, knowing chamber wall temperature will yield additional information on ion temperatures. Higher ion temperature leads to greater erosion of the channel wall, and this erosion is the main mechanism of Hall thruster failure when the magnetic coils become exposed to the plasma flow (13). Thus, knowing anode channel wall temperature will potentially allow researchers to relate operational temperature to erosion and eventual thruster failure.

Thermal Imaging Option

Capturing thruster temperatures needed a non-intrusive means of collecting data due to the operation of the thruster within a vacuum chamber and the high cost of a thruster, along with the desire to collect temperature data over the entire visible surface of the thruster. While thermocouples are an established means of capturing object temperatures, and are relatively simple to use, there are drawbacks to using them. One drawback is the need to physically attach the thermocouples to the object, which is destructive to the item being monitored if a strong adhesive or welding is used. This may also cause temperature inaccuracies due to their perturbation of local temperatures, particularly for small items. Adhesives do not always provide the best thermal contact to the object, and the thermocouple may come loose if the adhesive fails. Observing a Hall thruster operating in a vacuum chamber compounds the problem because repairs to the thermocouples or their attachment would require bringing the chamber back up to atmospheric pressure. Bringing the chamber up to atmosphere and opening it can take about 8 hours, and once the thermocouple work is completed, the chamber must be depressurized back to vacuum, consuming eight additional hours. Mechanically attaching the thermocouples might require physically altering the thruster, which may affect future experiments, or it might be somewhat destructive to the thruster, which is undesirable due to the high cost of the thruster. In addition, thermocouples only provide temperature readings of the specific part of the thruster to which they are attached. Thermal imaging, however, would require no modification of the thruster, would not require vacuum chamber opening and closing to correct any imaging problems, and would provide temperature data over the entire visible surface of the thruster. There are

drawbacks to thermal imaging, such as the complexity of correcting the raw data to actual temperatures, and the higher cost of operating a thermal imaging system. However, thermal imager vendors have largely addressed the inherent data manipulation needed to obtain corrected temperatures, and the one time cost of the imager is lower than the cost of continuously replacing thrusters.

Radiation and Thermal Imaging Basics

Since thermal imagers convert incident radiation to a temperature reading, a discussion of the pertinent topics concerning radiation is appropriate. Radiation is energy emitted in the form of electromagnetic waves and is normally characterized over a band of wavelengths ranging from 10^{-8} μm to 10^{10} μm (14). Thermal imagers are generally sensitive to the infrared band between 2 μm and 13 μm (15). The radiation received by a thermal imager is dependent on several factors, including: distance between the camera and the object, object emissivity, transmissivity of intervening mediums, and temperature of any reflecting objects. The distance between the camera and the object affects the radiation received because as radiation is emitted, it spreads out evenly and the power of the radiation is reduced. If the power of the radiation emitted is high compared to the distance traveled, the affect will be small. This assumes the radiation source is diffuse, which means the radiation emitted is equal in all directions. The emissivity of an object refers to how well the object radiates energy as compared to a black body. The radiation emitted by a black body is only a function of its temperature and thus has an emissivity of 1, while real objects have an emissivity less than 1. The emissivity, e, of an object depends on temperature, wavelength of emitted energy, and angle of emission (14:41). The transmissivity, t, of a medium refers to how much of the incident radiation is

transmitted through the medium. A transmissivity of 1 indicates all of the incident radiation is transmitted, while a value of less than 1 indicates a fraction of the radiation was absorbed or scattered by the medium (14:423). Objects other than the one studied emit radiation that is reflected off the studied object and received by the camera. The camera temperature measured would increase due to this effect, thus creating a falsely high object temperature reading.

While the camera software accounts for a reflected temperature of the surroundings, the inside of the vacuum chamber in this case, it does not account for this type of interaction between the thruster components. This invokes an introduction on the idea of "configuration factor" also known as "view factor", which is the fraction of uniform diffuse radiation leaving a surface that directly reaches another surface (14: 156). For example, the radiation received by the camera from the cathode is a result of the cathode itself emitting radiation and radiation leaving the thruster body, being reflected off the cathode and finally reaching the camera. Object geometry, relative orientation of the two objects, and the distance between the objects determine the view factor. Determining the view factor for the thruster components using the integral methods found in reference literature would be exceedingly complex due to the component geometry and orientation, and despite a number of existing derived configuration factors (14, 16), none closely matched the thruster component configuration. Computer programs exist that may allow view factors to be accurately determined (17, 18), however, they were not used here due to time constraints and are suggested as a future work. All of these factors affect the radiation received by the thermal imager and should be considered to obtain the most accurate object temperature data.

At the most basic level, a thermal imager works by detecting incident thermal radiation and converting it to a temperature. A thermistor bolometer, for example, consists of a material, usually carbon, germanium, or a mixture of metal oxides (19:148) whose resistance varies with temperature. The temperature of the receiving material will depend on the amount of incident radiation energy absorbed from the source observed as shown in Figure 9.

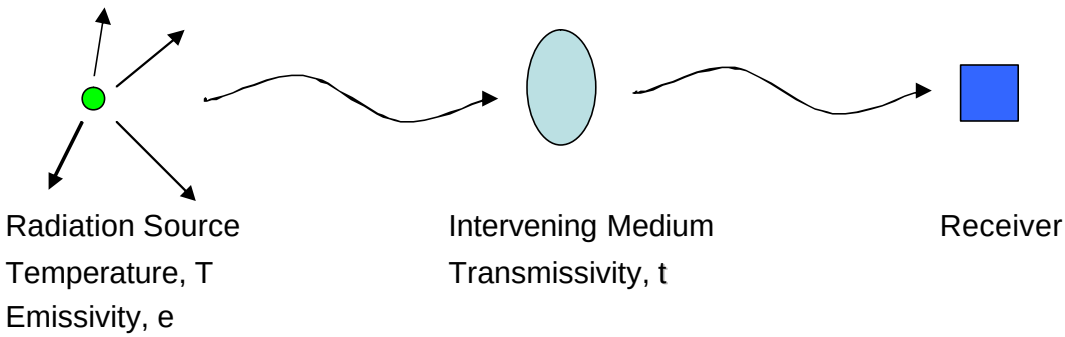

Figure 9: Basic radiation schematic

The intensity of the radiation received will depend on the temperature of the source, the emissivity, and the transmissivity as discussed earlier:

$$Instensity Received = tesT^4 \qquad (1)$$

The Steffan-Boltzmann constant, s, is needed for unit conversion. The intensity received is radiation energy that changes the temperature and thus the resistance of the receiver material. The camera electronics and software can then convert the change in resistance to a temperature reading.

The incident radiation, and therefore temperatures the camera measures actually come from several sources in practical situations. The camera software can account for these factors as shown in Figure 10 (20:183).

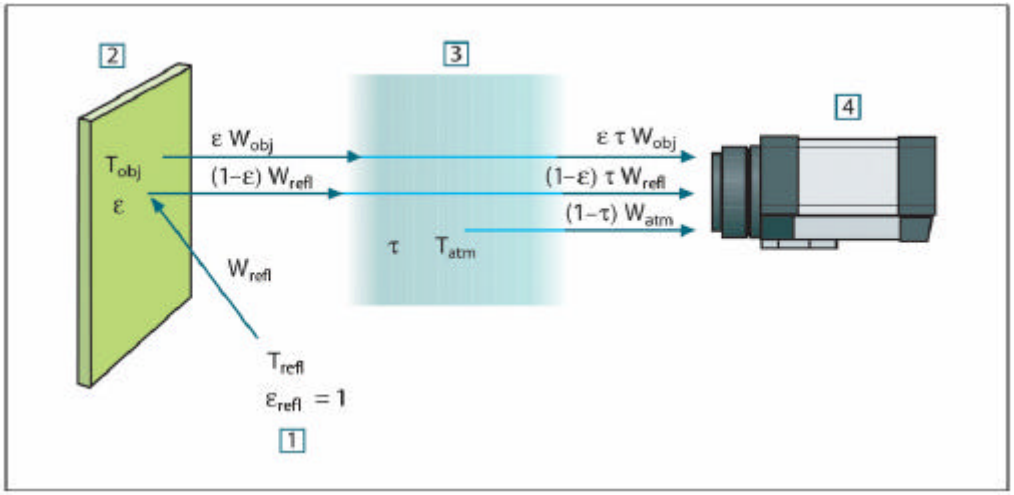

Figure 10: Schematic of thermographic imager measurement (20:183)

The three sources of radiation sensed by the camera are: the object, sources whose emitted radiation is reflected off the object, and the atmosphere between the camera and the object. The total received radiation power is:

$$W_{tot} = etW_{obj} + (1-e)tW_{refl} + (1-t)W_{atm} \qquad (2)$$

The radiation sensed, $W = sT^4$, is converted to a voltage, U, within the camera, which is used to calculate the temperature of the object as shown in the following equation (20:186):

$$U_{obj} = \frac{1}{et} * U_{tot} - \frac{1-e}{e} * U_{refl} - \frac{1-t}{et} * U_{atm} \qquad (3)$$

where U_{obj} is the calculated camera output voltage for a blackbody of temperature T_{obj} (i.e. a voltage directly converted into true requested object temperature). U_{tot} is the measured camera output voltage for the actual case. U_{refl} is the theoretical camera output voltage for a blackbody of temperature T_{refl} according to the calibration. U_{atm} is the theoretical camera output voltage for a blackbody of temperature T_{atm} according to the calibration, e is the emissivity, and t is the transmissivity. The camera software accepts

input values for: distance between the camera and the object, object emissivity, transmissivity, temperature and humidity of the atmosphere and temperature of the reflecting object. The resulting temperature data generated by the camera software exports to an output file for further post processing.

Thermal Imager Used

Several factors influenced camera selection, including camera cost, temperature and wavelength range, resolution, and viewing capabilities for the experimental setup. The wavelength range coverage required was 7.5 μm to 13 μm and a model with a higher resolution was more desirable if not cost prohibitive. The viewing capabilities, to include the minimum focus distance, had to allow for the dimensions of the thruster and the distance between the camera and thruster in order to maximize the area of the screen taken up by the thruster. Several cameras produced by FLIR, Inc were researched, and the two models fitting the need for the experiment were the ThermaCam Merlin and the ThermoVision A40M. Table 3 shows a comparison of the two cameras.

Table 3: Thermal Imaging camera comparison

	Model	
	A40M	**Merlin**
Purchase Price (Researcher Software Included)	$ 43,950	$ 73,500
Rental Price = 10% (per month)	$ 4,395	$ 7,350
Lease Price (over 12 months)	$ 11,964 X 4 payments = $ 47,856 Or $ 1,510 X 36 payments = $ 54,360	Not requested.
Temperature Range (K)	273°K to 773°K Optional Up to 1773°K or 2273°K	273°K to 623°K Optional 573°K to 1773°K
Resolution	320 x 240 = 76,800 pixels	320 x 256 (5210 or 6% more pixels)
Accuracy	±2°C or ±2% of reading	±2°C or ±2% of reading
Wavelength Range (µm)	7.5 to 13	1.5 to 5.5
PC connection	RS232 and Firewire	RS232
Video Out	Composite	RS422, S-video
Lens FOV / min focus distance	24° x 18° / 11.8 in	11° x 8° (50mm) / 20 in
Additional Lens / min focus distance	12° / 47.2 in	N/A

The A40M had the advantage of covering a wider stock temperature range, 273 to 773 K vs. 273 to 623 K for the Merlin, while providing nearly the same resolution, and a cost of just under 50% of the Merlin. Additional hardware in the form of filters would be required to accurately read temperatures above 773 K. For these reasons, the A40M shown in Figure 11 was chosen for the experiment.

Figure 11: FLIR, Inc, ThermoVision A40M (20)

The camera provides for image capture control on the camera itself, and with the ThermaCam Researcher Software, discussed earlier. The camera connects to a PC via fire wire in order to provide data output.

Thermal imagers also used in industry

In 1995, researchers studied a UK-10 grid type ion thruster using a 128 x 128 pixel thermal imager (21). In addition, thermal imagers today are used in a wide range of applications by many different industries (22), demonstrating a level of acceptance as an investigative technology. One example is analyzing heat distribution in catalytic converters by major automotive manufacturers. Another is the detection of plugged cooling fins on a heat exchanger, which is easily detectable based on the different temperatures of the fins represented by the different colors in Figure 12.

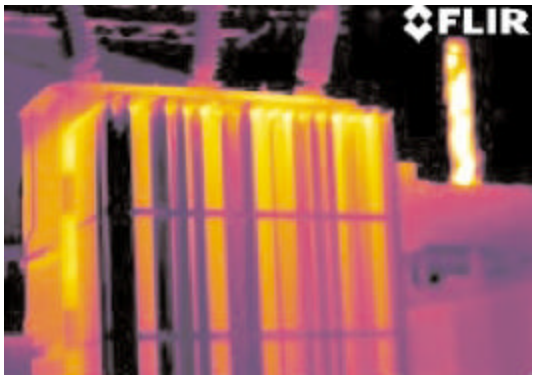

Figure 12: Plugged cooling fins in a heat exchanger (23).

The last example is fault detection in a component at a power station. The fault is not detectable visually except when viewed with a thermal imager (see Figure 13).

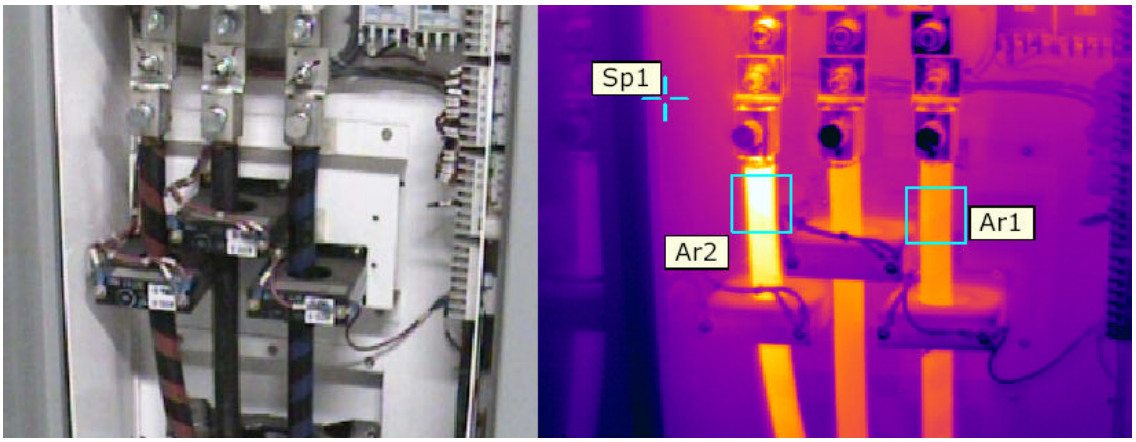

Figure 13: Power plant component (left) and thermal image (right) showing fault in Ar2 (24:3).

These applications as well as a multitude of others can be found associated with camera manufacturers indicate heavy use of infrared camera technology.

Error Analysis Approach

A parametric approach determined error associated with factors such as camera accuracy, software number rounding of distance measurements, transmissivity for the window and the atmosphere, reflected temperature, and emissivity value used for the various materials. The advantage was that each input value varied individually according to the band of values known for that parameter, and the output temperature changed from

the lowest possible value to the highest possible value as a result. Once the resulting temperature band for each input value was found, an additional method was used to combine the errors in a way to reveal a combined affect. Therefore, two sets of temperature data were produced for each material: one used all of the input values for each parameter resulting in the lowest temperature reading, and one used all of the input values for each parameter resulting in the highest temperature reading. By comparing the temperature difference, an overall output temperature band of error, i.e. ± degrees K, was found based on the area of the thruster being analyzed. A statistical approach used to find standard deviation included measuring any temperature changes at different points on the thermal images captured during the period with the thruster under steady state conditions. A discussion with specific numbers used is contained in the Data Analysis section of the Methodology.

III. Methodology

Chapter Overview

First in this chapter is a description of the specific components used in this experiment, including a discussion on the reasoning behind the values used as input for the camera software. Next is a description of the laboratory setup followed by a summary of the data collected, with a breakdown of the different thruster operating conditions observed. Last is the data analysis methodology followed by the error analysis completed.

Hall thruster

The Hall thruster used was the Busek BHT-200-X3 laboratory model, which is a 200W Hall thruster of the same type shown in Figure 14 (5).

Figure 14: Busek BHT-200-X3 Hall Thruster (5)

The thruster used in this experiment was not new and had an unknown number of hours of use experienced. The thruster showed evidence of use in its appearance as a result. There was a dark discoloring and iridescent appearance in the anode channel and all over the steel portions of the thruster as shown in Figure 15 and Figure 16.

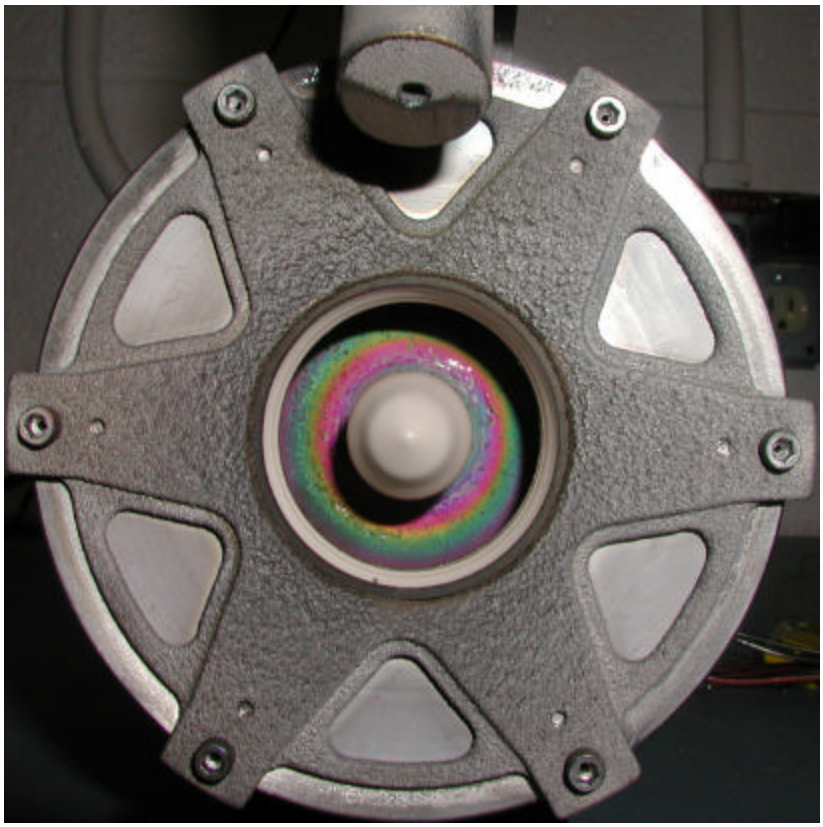

Figure 15: Exit plane and anode chamber discoloration

In Figure 16, the entire thruster shows a bronze discoloration, except for the mounting bracket on the left, cleaned after the experiment.

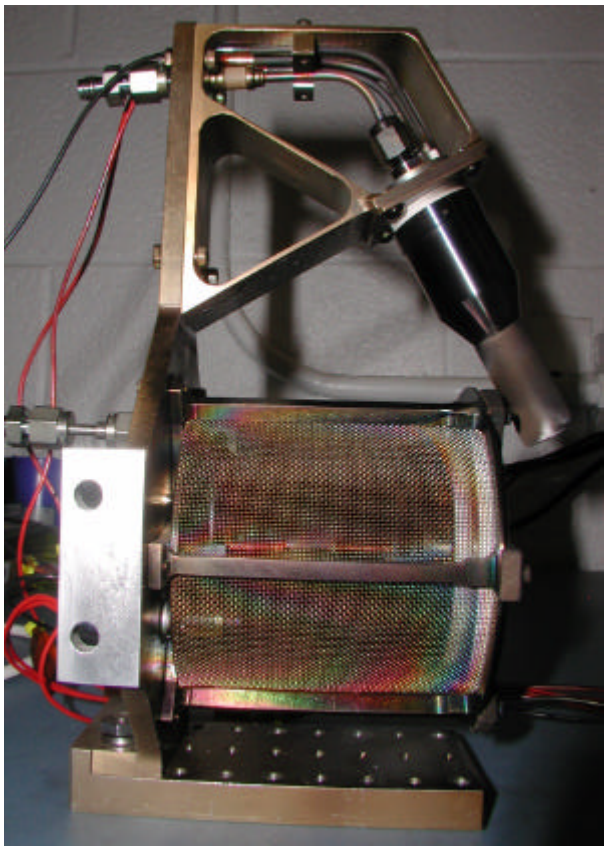

Figure 16: Thruster discoloration.

The discoloration was removed by lightly cleaning the mount with a wire brush. Also, note the discoloration of the cathode in comparison to a brand new thruster seen in Figure 6. This discoloring is important since emissivity is, in part, a function of the coating of a surface with another material (14: Ch 4). If there were an oxide layer present, this would increase emissivity by as much as five times (16: Ch 12). This impacted the values used for the emissivity of the various parts of the thruster. Reference values of emissivity for various types of steel are in Table 4 (14:836-838, 16:929-931).

Table 4: Values of Emissivity for selected types of steel

	Emissivity	Temperature or Temperature Range (C)
Stainless Steel	0.23	200
Stainless Inconel X Polished	0.19 to 0.20	-183 to 486
Stainless Inconel X Polished	0.19 to 0.22	-183 to 486
Stainless 301 Polished	0.16	26
Stainless 310 Smooth	0.39	817
Stainless 316 Polished	0.24 to 0.31	707 to 1037
Stainless Steel Lightly Oxidized	0.33	500
Stainless Steel Highly Oxidized	0.67	500

The large variation in values highlights the importance of knowing the actual emissivity of the material studied since this will produce a potentially large variation in temperature readings. The value actually used was determined during the experiment as discussed in the Data Analysis section of this chapter. The values of emissivity used for the boron nitride anode cone and the alumina plasma sprayed portion of the cathode tip and exit plane were those for an unused thruster as provided by the manufacturer since actual values could not be determined during experimentation. The actual value determination was precluded due to the very high temperatures of the parts as compared to the capability of the thermocouples and additionally, in the case of the anode cone, the location within the plasma.

Vacuum Chamber

The vacuum chamber used in the experiment was Chamber 6 at the Air Force Research Laboratory located at Edwards Air Force Base, California. It is 1.8 m in

diameter and 3 m long with a measured pumping speed of ~ 32,000 l/s on xenon. The initial vacuum is provided by a pump and blower system, while the final vacuum is provided by four single-stage cryopanels maintained at approximately 25 K and one two-stage cryopump maintained at roughly 12 K. A top-down view of the chamber is shown in Figure 17.

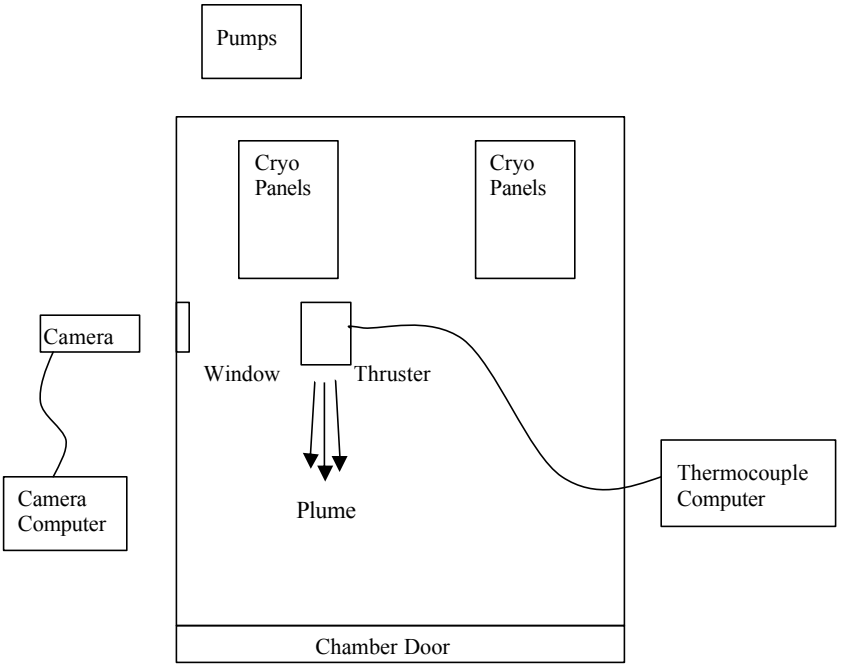

Figure 17: Schematic top down view of vacuum chamber setup

Thermal Imaging Camera

The lab setup included the FLIR, Inc ThermoVision A40M thermal imager outside the chamber and connected to a computer via fire wire. A felt cover placed around the gap between the camera lens and the zinc-selenide window reduced the influence of outside sources of light.

Window

Since the experiment took place with the thruster operating in a vacuum chamber, and the thermal imaging camera was placed outside the chamber, an appropriate viewing

window was needed. The window needed to fit the existing chamber view ports and allow the 7.5 µm to 13 µm wavelength radiation to pass through. The research lab already had a zinc-selenide (Zn-Se) window available, but a larger size 0.102 m (4 inch) view port was researched to allow for the possibility of accommodating larger diameter thermal imaging camera optics. Larger windows of this type were cost prohibitive at approximately $3000 each and required extensive lead-time for delivery. In addition, this cost covers only the window itself, so additional manufacturing would have been required to create a window housing useable in the vacuum chamber view ports. For these reasons, the existing Zn-Se window was used. The window is partially visible in the overexposed image in Figure 18.

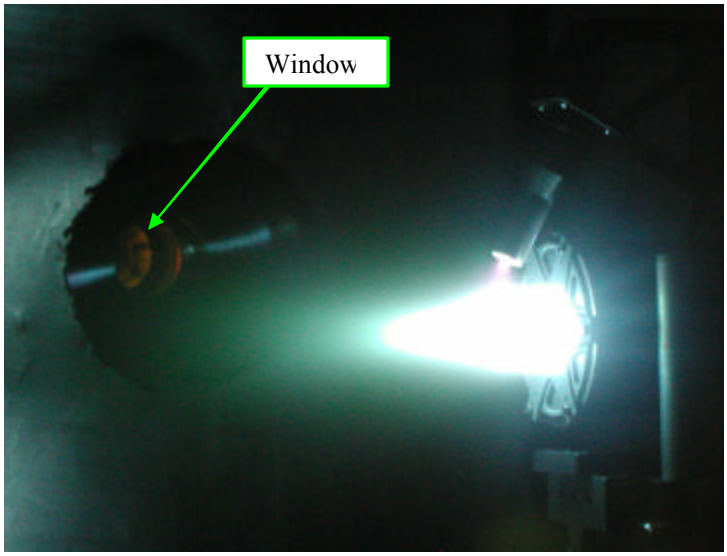

Figure 18: Zinc Selenide Window During Thruster Operation

Camera Software

ThermaCam Researcher was the software provided by the thermal imaging camera manufacturer, FLIR, Inc, interpreting the data coming from the camera and allowing for display of the image, as well as saving each frame of data in a proprietary format for later analysis. The software also provided for real time data analysis and the

adjustments needed for the experiment. The adjustments to the raw camera data include: object emissivity, distance between the camera lens and the object, reflected temperature, atmospheric temperature and humidity, and optics transmissivity. Object emissivity refers to the thruster in this case, yet the emissivity varies for the different materials used for each thruster component. While the user can identify different areas of the image and individual emissivity values can be set for those areas, when the entire image is output for data manipulation, the software uses only the "object emissivity" to calculate the resulting temperatures. If only a selected area of the image is output for data manipulation, then the emissivity set for that area is used instead of the "object emissivity". Therefore, if a composite image showing the temperatures corrected for all of the different emissivity values over the entire thruster is desired, then post processing of the data is required. Such post processing included data manipulation and error analysis by first creating composite images of the entire thruster. These images were actually Matlab surface plots of the temperature data output by ThermaCam Researcher.

Overall Lab Setup

The overall lab setup consisted of mounting the thruster at an optimum viewing position inside the vacuum chamber and viewing the thruster from outside the chamber through the Zn-Se window with the thermal imaging camera. The setup as viewed from the chamber door is shown in Figure 19.

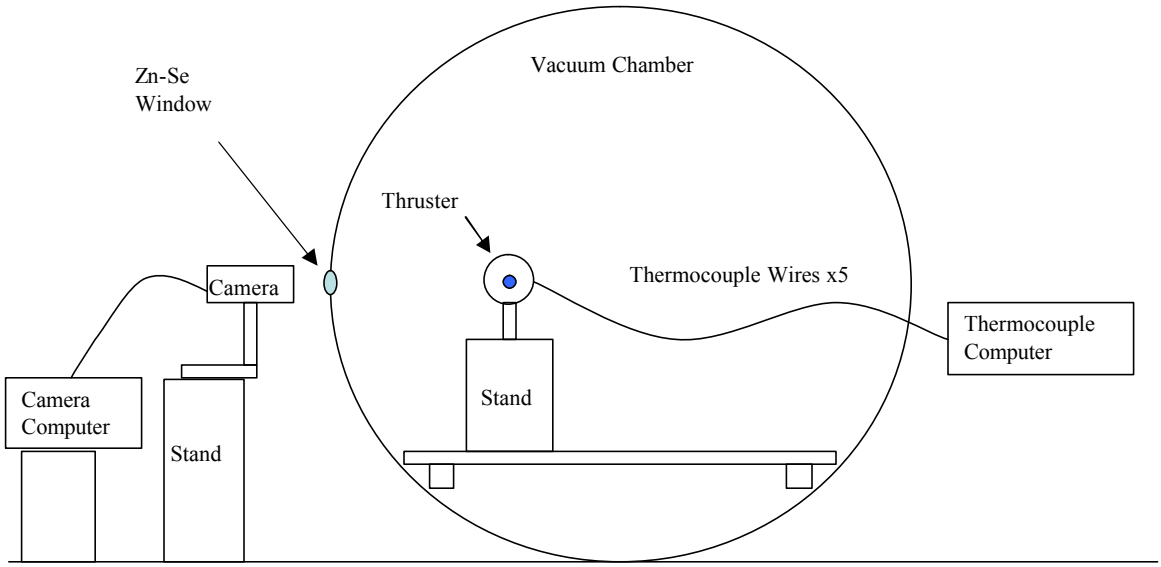

Figure 19: Chamber and Test Setup

The computer attached to the camera via fire wire was a standard Microsoft Windows based personal computer running the ThermaCam Researcher software. The computer attached to the thermocouples used LabView® to monitor the thermocouple data. The five thermocouples were attached at various points on the thruster and to the inner chamber wall in order to compare the temperature value output by the camera to a temperature measured by more conventional means (see Figure 20).

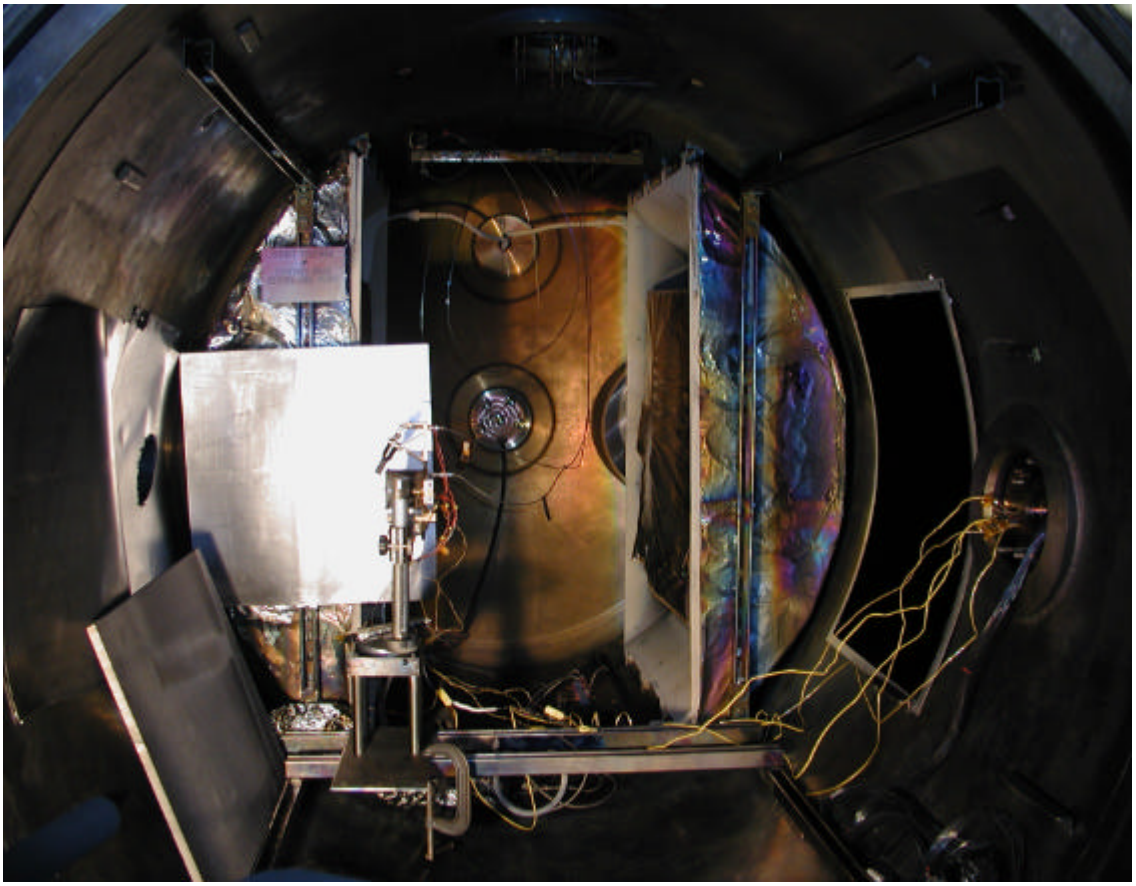

Figure 20: Thruster and yellow thermocouple wires inside Chamber 6.

Four thermocouples were attached directly to the thruster, with three fixed by epoxy and one by Kapton tape. Epoxy fixed a fifth thermocouple to the inner vacuum chamber wall. The exact thermocouple locations were: #1 on the metal axial support bar in the center of the thruster on the side opposite the camera, #2 on the metal support at the rear of the thruster on the side opposite the camera, #3 on the inner chamber wall 0.33 m (13 in) below the Zn-Se window and 0.08m (3 in) further from the chamber door than the window centerline, #4 on the cathode support mount near the thruster/mount interface, and #5 on the metal support at the rear of the thruster on the side facing the camera. Due to the need to protect the chamber walls while the thruster was firing directly toward the camera, mylar sheets were put in place to cover portions of the chamber wall as shown in Figure 20.

The thruster was placed at a distance of 0.673 m (26.5 in) from the Zn-Se window in order to maximize the number of camera pixels covering the thruster. At this distance, the thruster took up approximately 44% of the 320 pixel x 240 pixel image area, or approximately 33,776 pixels. Adding the window thickness of approximately 0.003 m (0.1 in) and the distance between the window and the camera lens of approximately 0.043 m (1.7 in) meant the total distance between the camera lens the centerline of the thruster was 0.72 m.

Data Collection

Data was collected on September 26-27, 2006 and included thruster operation during start up, shut down, and steady state conditions. The thruster was considered to have achieved thermal steady state when the temperature measured at several points on the thruster exhibited a one-degree temperature change in 30 minutes. The thruster was also rotated from a position where it was viewed from the side with the exit plane facing the right, through 90° to a position where the exit plane was facing the camera. The vacuum chamber pressure was approximately 4×10^{-5} Pa (3×10^{-7} Torr) while the thruster was firing. The ThermaCam Researcher software captured each frame of temperature data for later analysis. Table 5 shows a summary of the experimental thruster conditions for which data was captured.

Table 5: Data Collection Summary

Date	Time	Thruster Condition	Xenon Flow Rate (sccm)	Duration (hrs)
26 Sept 2006	1234 - 1620	Start up to steady state	8.50	3.75
	1620 – 2120	Shut down	0	5.00
27 Sept 2006	0804 – 0830	Start up	8.50	0.50
	0830 – 0834	Running with exit plane facing camera	8.50	0.10
	0835 – 0948	Shut down	0	1.20
	0958 - 1330	Start up to steady state	7.00	3.50
	1331 - 1607	Running	10.0	2.60
	1610 - 2010	Shut down with exit plane facing camera	0	4.00

Data Analysis

Thruster side view heat up, steady state, and cool down

In the ThermaCam Researcher software, four spot temperature locations were chosen, and the temperature data for each location was output in order to determine the change in temperature over time as the thruster heated up. The four locations along with the ThermaCam Researcher spot name and X and Y positions were: steel axial support bar near the exit plane (SP01, X1:145, Y1:161), boron nitride cone at the end of the anode channel (SP02, X1:159, Y1:155), upper steel portion of the cathode (SP03, X1:148, Y1:67), alumina plasma sprayed lower portion of the cathode (SP04, X1:169, Y1:105) (see Figure 21).

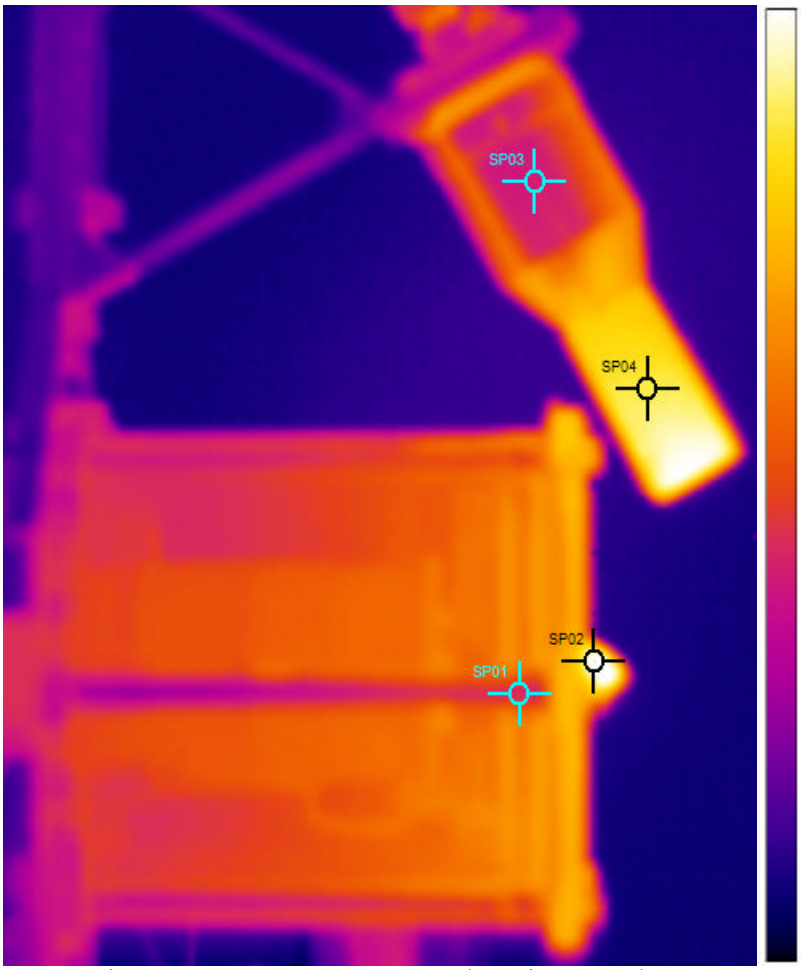

Figure 21: Spot temperature locations on thruster

The values used for "object parameters" shown in Table 6 include an emissivity value of 0.2, determined by varying the emissivity setting within the Researcher software until the temperature displayed matched the thermocouple #5 in the same area. Note this is twice the value of the stainless steel emissivity value provided by the manufacturer for a new thruster. This is likely due to the discoloration and coating discussed earlier and suggests the emissivity values provided by the manufacturer, while correct for a new thruster, may be lower than the actual values on a thruster with accumulated operating time. The emissivity for the anode cone was set to 0.45 under the settings for SP02. The 0.45 emissivity value represents a value for the boron nitride of a new thruster as provided by

the manufacturer. The emissivity for the cathode tip was set to 0.23 for SP04, which also represents a value for the alumina plasma sprayed portion of the cathode of a new thruster as provided by the manufacturer.

Table 6: Object Parameter settings in ThermaCam Researcher

	Value		Value
Emissivity	0.20	**External Optics Transmissivity**	0.62
Distance (m)	0.7	**Atmosphere Temperature (C)**	21
Reflected Temperature (C)	18	**Atmosphere Relative Humidity (%)**	50
External Optics Temperature (C)	21	**Researcher Calculated Atmosphere Transmissivty**	0.99

Temperature and time values for 60 data points during the heat up and 71 data points for cool down were used to ensure enough data to capture the heating and cooling rates. For the plots generated, the initial time was set to zero min and the number of minutes elapsed between each data point was noted and added to the time for the last data point. One image, ThermaCam Researcher file tc0501.fff, was chosen for steady state temperature analysis based on temperature trend analysis showing very small changes in temeperature. Although this image contains temperature data for the entire thruster, analysis focused on the axial support bar near the exit plane, the cathode, the anode, and the magnet core area.

Thruster exit plane view temperatures and cool down

The rotation of the thruster allowed for a view of the cathode channel and exit plane. An image containing the anode channel was captured with the exit plane at a 45° angle to the camera. The values set within ThermaCam researcher are shown in Table 7.

Table 7: Object Parameter settings in ThermaCam Researcher for Anode

	Value		Value
Emissivity	0.45	**External Optics Transmissivity**	0.62
Distance (m)	0.7	**Atmosphere Temperature (C)**	21
Reflected Temperature (C)	18	**Atmosphere Relative Humidity (%)**	50
External Optics Temperature (C)	21	**Researcher Calculated Atmosphere Transmissivty**	0.99

The emissivity was set to 0.45 to account for the boron nitride.

A second image was taken with the exit plane directly facing the camera. The temperature data from ThermaCam Researcher image tc1220.fff was corrected for the different material emissivity values. The values set in ThermaCam Researcher are in Table 8.

Table 8: Object Parameter Settings in ThermaCam Researcher for Exit Plane Facing Camera

	Value		Value
Emissivity	Varied	**External Optics Transmissivity**	0.62
Distance (m)	0.7	**Atmosphere Temperature (C)**	21
Reflected Temperature (C)	18	**Atmosphere Relative Humidity (%)**	50
External Optics Temperature (C)	21	**Researcher Calculated Atmosphere Transmissivity**	0.99

There were three images required to create a composite image with the corrections needed for the different emissivity values of the boron nitride, alumina plasma spray, and the steel. This was necessary since the ThermaCam Researcher software does not display the emissivity corrected temperatures in the image when more than one emissivity is used, rather it shows the corrected values numerically in a separate text field. It also will not output the corrected data containing temperatures with several emissivity corrections.

ThermaCam Researcher will not display in a composite image, or output composite data corrected with more than one emissivity set. So in order to create a composite image displaying the temperatures in the image as corrected with different emissivity values, the numerical data from ThermaCam Researcher must be output with one emissivity set for the entire image. Post processing the images assembled the different parts into a single image with corrected temperatures. So first, the emissivity was set to .23 for the alumina plasma spray, and the data was output. Next, the emissivity was set to 0.20 for the steel, and the data was output. Last, the emissivity was set to 0.45 for the boron nitride, and the data was output. This resulted in three data sets of temperature data in matrix form. The matrix of temperature values from the image corrected for the alumina plasma spray was used as a base matrix since most of the image area contained thruster parts with the alumina plasma spray, namely the face of the exit plane and the cathode tip. Next, the matrix data from the image corrected for the steel emissivity was copied and pasted over the data in the first matrix for the upper steel portion of the cathode. Last, the matrix data from the image corrected for the boron nitride was copied and pasted over the data in the first matrix for the area of the anode channel and anode cone. The result was a matrix of temperature values used to generate a surface plot so a composite image could be seen.

The last data analysis consisted of measuring the cooling rate with the exit plane facing the camera. Four spot temperatures were set within ThermaCam Researcher: SP01 on the anode cone (X1:157,Y1:157), SP02 on the anode rear channel wall (X1:157,Y1:144), SP03 on alumina plasma sprayed portion of the exit plane (X1:186,Y1:156), and SP04 on the Cathode tip (X1:157,Y1:122) as shown in Figure 22.

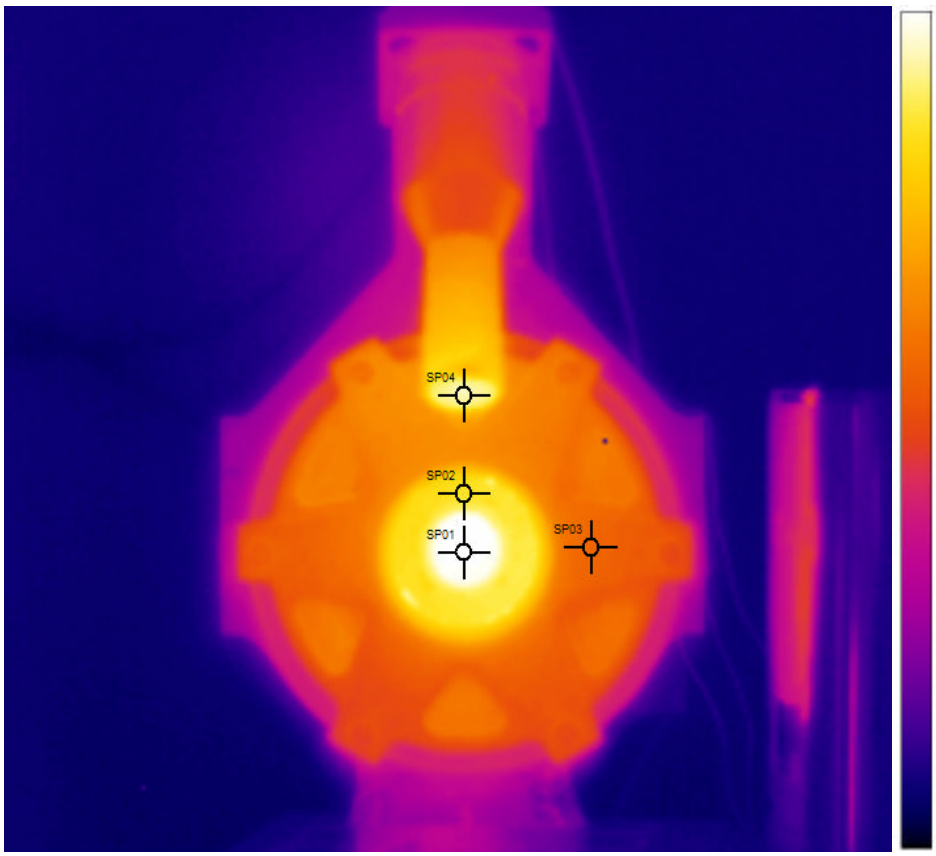

Figure 22: Spot Locations for Cool Down Data with Exit Plane Facing the Camera

The ThermaCam Researcher settings are shown in Table 9.

Table 9: Object Parameter settings in ThermaCam Researcher for Cool Down with Exit Plane Facing Camera

	Value		**Value**
Emissivity	0.65	**External Optics Transmissivity**	0.62
Distance (m)	0.7	**Atmosphere Temperature (C)**	21
Reflected Temperature (C)	18	**Atmosphere Relative Humidity (%)**	50
External Optics Temperature (C)	21	**Researcher Calculated Atmosphere Transmissivty**	0.99

The emissivity value of 0.65 was chosen to lower the temperatures of the image in an attempt to capture as much data as possible within the ~773 K maximum temperature capability of the camera. Since the change in temperature values over time, rather than

actual temperature values, is needed for cooling rate data, this does not impact the result. In the plots, the initial time was set to zero min and the number of minutes elapsed between each data point was noted and added to the time for the last data point.

Uncertainty Analysis

Many factors could introduce error. The most notable include: camera accuracy, stated by FLIR, Inc. is ± 2 K, software number rounding of distance measurements, transmissivity for the window and the atmosphere, reflected temperature, and emissivity value used for the various materials.

It was noted during analysis the ThermaCam Researcher software rounds values for distance to the nearest 0.1 m, which means any distance entered as 0.11 to 0.14 will be rounded down to 0.1 and any value entered as 0.15 to 0.19 will be rounded up to 0.2. Although the measured distance for this experiment was 0.72 m, the value of 0.7 m was used by the software. The results were checked for sensitivity to this error by entering several values for distance and observing the resulting change in temperature. It was noted the distance had to be set to 5.0 m before a one degree difference in temperature was observed, thus indicating the results were not sensitive to distance errors for this experiment. This is probably due to the relatively small distance between the camera and the thruster compared to the thermal radiation emitted.

Data provided by a Zn-Se window manufacturer indicated that a Zn-Se window had a transmissivity of 0.62 over the wavelength range of 7.5 μm to 13 μm to which the camera is sensitive. Lab testing with a black body source indicated the window transmissivity used for the experiment may be as high as 0.68 in the temperature range of 425 K to 725 K. As such, window transmissivity varied between 0.56 and 0.68 in the

software resulted in a temperature change of ± 6 K. The air transmissivity value depends on atmosphere temperature and humidity. The calculated transmissivity of the atmosphere used in the experiment was 0.99 at 294 K and 50 % humidity. With the temperature and humidity varied, the resulting change in transmissivity and temperature was observed. With the humidity held constant at 50 % and the air temperature varied between 278 and 317 K, the transmissivity only varied between 0.99 and 1.0 and the resulting image temperature did not change. With the air temperature held constant at 297 K and the humidity varied between 20 % and 70 %, the transmissivity only varied between 0.99 and 1.0 and the resulting image temperature did not change.

For the purposes of this experiment, the reflected temperature was the temperature of the inner vacuum chamber wall. A thermocouple on the wall indicated a constant temperature of 291 K while the chamber was at vacuum with the thruster operating. However, due to the need to protect the chamber walls while the thruster was firing directly toward the camera, mylar sheets were put in place to cover portions of the chamber wall as shown in Figure 20. In addition, the vacuum chamber cryo-coolers would also present a different reflected temperature. For these reasons, the reflected temperature was varied between 283 and 299 K. The resulting calculated thruster temperature was observed. Based on the results and the thermocouple accuracy of ± 2 K, the potential error was ± 3 K.

As noted earlier, emissivity varies based on the material in question. It also varies based on other factors, including temperature, surface roughness, color, and whether or not the surface is a diffuse emitter. As a result, the preferred method of finding the actual emissivity would be to attach a thermocouple and compare the temperature reading with

the camera as emissivity is varied. When the temperatures match, the emissivity value can be noted. While this was done for the steel axial support bar, it was not done on the other materials due to the very high temperatures of the parts as compared to the capability of the thermocouples and additionally, in the case of the anode cone, the location within the plasma. In any case, the emissivity was varied for the three materials and the resulting temperature change was noted. Variations in emissivity of ± 0.05 of the actual emissivity resulted in temperature changes of ± 37 K for steel, ± 81 K for the alumina plasma spray, and ± 52 K for the boron nitride. The higher value for the alumina plasma spray over the value for the steel is due to the higher temperature of the alumina plasma spray. The value for the boron nitride is higher than both the steel and the alumina plasma spray due to a higher emissivity and higher temperature of the boron nitride as compared to the steel and alumina plasma spray.

As discussed earlier, an additional method was used to combine the errors in a way that would reveal a combined affect "worst case" temperature error range. Therefore, two sets of temperature data were produced for each material: one used the input values for each parameter resulting in the lowest temperature reading, and one used the input values for each parameter resulting in the highest temperature reading. Table 10 shows the input values used for the images.

Table 10: Lowest and Highest Input Values

Parameter	Input value to get lowest temperature reading	Input value to get highest temperature reading
Object Emissivity	Steel: 0.25 Boron Nitride: 0.50 Alumina Plasma Spray: 0.28	Steel: 0.15 Boron Nitride: 0.40 Alumina Plasma Spray: 0.18
Distance (m)	0.7	0.7
Reflected Temperature (K)	299	283
Window Transmissivity	0.68	0.56
Atmosphere Transmissivity	0.99	0.99

Although the distance measured during experimentation may vary by ± 0.006 m (0.25 inch), the camera software rounds the input value to the nearest ± 0.1 m, therefore the input value for the distance remained constant. Similarly, the atmospheric transmissivity calculated by the camera software did not vary over the range of atmospheric temperatures and humidity used, thus the input value was held constant. The resulting minimum and maximum temperature was monitored for an area on the thruster containing each material. Subtracting the minimum temperature from the maximum temperature and dividing by 2 determined the temperature error range. With steel temperature reaching the 500 K range, and the boron nitride and alumina plasma sprayed parts of the thruster potentially above 700 K these values represent an 8 % to 12 % error shown in Table 11.

Table 11: Maximum Temperature Error Using Combined Input Values

Area	Maximum Temperature Error (K)	Maximum Temperature Error (%)
Steel	± 47	10
Boron Nitride	± 55	8
Alumina Plasma Spray	± 83	12

These numbers reasonably agree with a simple summation of the individual errors discussed earlier as shown in Table 12.

Table 12: Maximum Combined Temperature Error Using Simple Summation

Error Source	Temperature Error (K)	Temperature Error (K)	Temperature Error (K)
Camera	± 2	± 2	± 2
Window Transmissivity	± 6	± 6	± 6
Reflected Temperature	± 3	± 3	± 3
Emissivity (Material)	± 37 (Steel)	± 52 (Boron Nitride)	± 81 (Alumina Plasma Spray)
Sum	Steel: ± 48	Boron Nitride : ± 63	Alumina Plasma Spray: ± 92

The statistical analysis of 60 temperature values for two points on the thruster during steady state operation revealed a standard deviation of less than 2 K. The average temperature of the two points was 529 K and 498 K respectively. Appendix B contains detailed data used in determining error.

IV. Results and Discussion

Chapter Overview

In this chapter, the first section contains the results of the side view heating rate analysis, followed by side view steady state image temperatures and the side view cooling rate analysis results. The next section discusses the results of the steady state temperature analysis with the thruster exit plane at a 45 degree angle toward the camera, followed by the steady state temperature results of the thruster exit plane directly facing the camera. The last section contains cooling rate results with the thruster exit plane directly facing the camera. For reference, Figure 23 shows a picture of the thruster next to a raw thermal image with several components labeled.

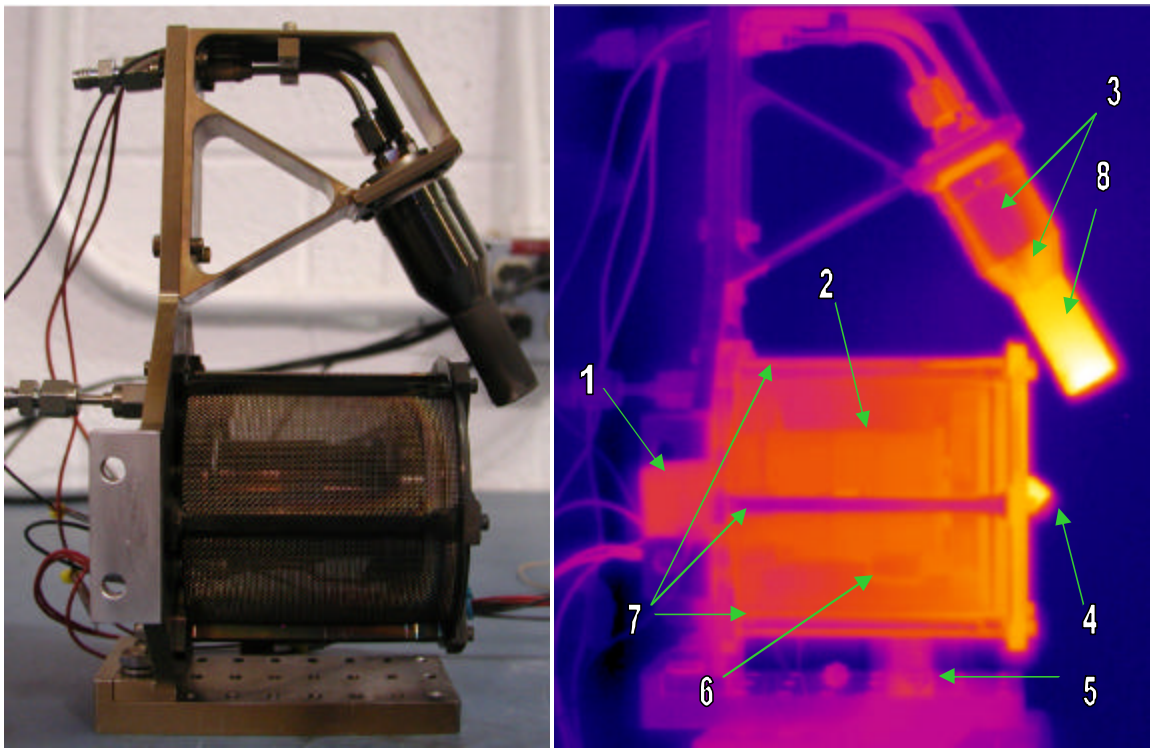

Figure 23: 200W Thruster and Researcher raw thermal image. (1. Kapton tape covering thermocouple #5. 2. Magnet core. 3. Steel portion of Cathode. 4. Anode cone. 5. Reflection from rear stand on thruster mount plate. 6. Power wire for anode. 7. Axial support bars 8. Alumina plasma sprayed portion of the Cathode.)

Heating rate results taken from thruster side view images

The following heating rate results were taken from the data gathered following thruster start up to 8.5 sccm. Figure 24 shows a plot of temperature change vs. time for the axial support bar near the exit plane, which was spot SP01 in Figure 21.

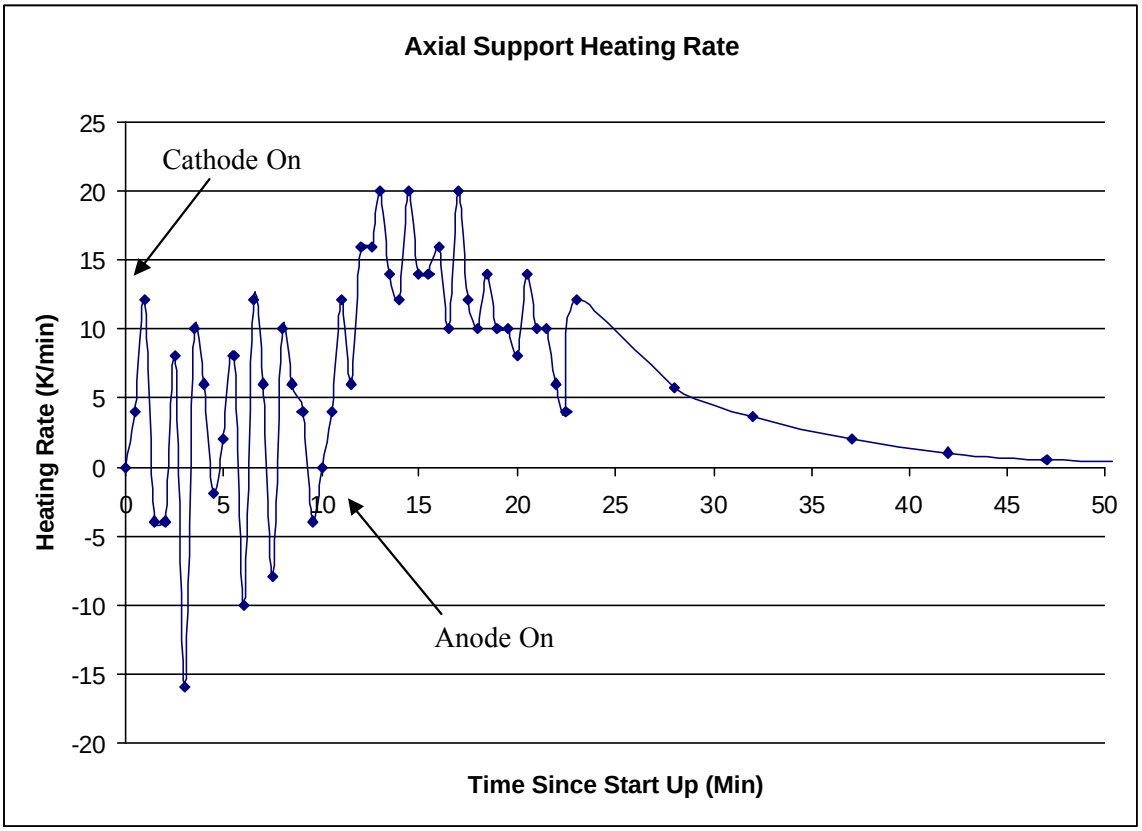

Figure 24: Axial Support Heating Rate

The time since start up indicates the amount of time elapsed after the cathode was conditioned and anode flow began. The heating rate varies between 0 and 10 degree K per minute for the first 10 min, then varies between 10 and 20 degrees K per minute between 12 and 25 min after start up. The apparent oscillation of the heating rate during the first 10 minutes was due to very small temperature changes over the time interval observed. The heating rate is less than 1 degree K per minute about 42 min after start up. The increase in heating rate at the 10 min mark coincides with an increase in heating rate

of the anode cone (Figure 25). This is probably due to the heating of the anode section from the xenon plasma and subsequent conduction from the higher temperature anode section outward to the other areas of the thruster. Another possibility is that as the thruster begins to fire and plasma is formed at the exit, some of the xenon is impacting the alumina plasma sprayed portion of the exit plane of the thruster, which then conducts the heat to the axial support bars. While radial xenon neutral velocity is nearly zero at the exit plane, the velocity increased to an average of 75 m/s just 10 mm (0.39 inch) from the exit plane (25). Therefore, the increase in heating rate of the axial support bar may indicate xenon affecting thruster temperatures. Figure 25 shows the heating rate for the anode cone, which was spot SP02 in Figure 21.

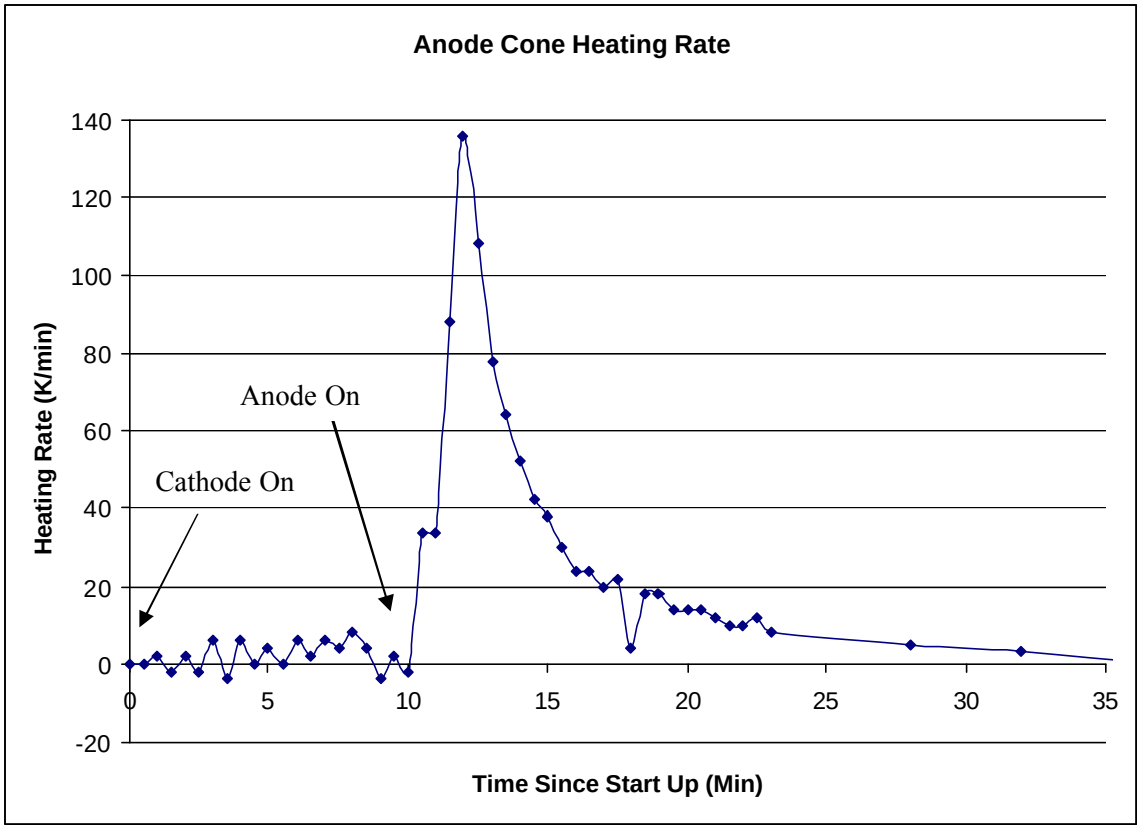

Figure 25: Anode Cone Heating Rate

The heating rate appears to be insignificant until 10 min after start up, then increases sharply to 138 K/min before coming back down to less than 40 K/min at about 15 min after start up. The heating rate lowers to about 3 K/min at 32 min after start up, then appears to go to 0 K/min after 30 min. It does not actually reach 0 K/min at this point because the temperature reading reached ~ 773 K, which is the maximum value measurable by the camera. Figure 26 shows the heating rate for the steel portion of the cathode, which was spot SP03 in Figure 21.

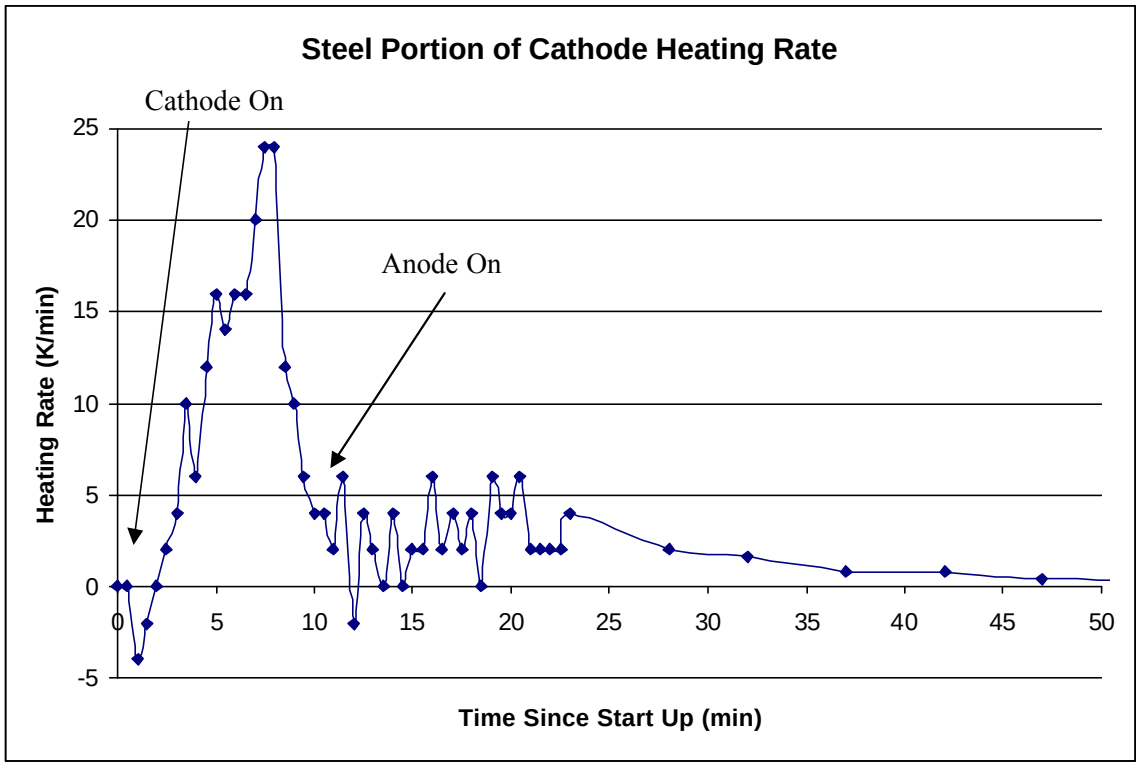

Figure 26: Steel Portion of Cathode Heating Rate

Here, the heating rate increases rapidly during the first 8 min following start up, then stabilized between 3 and 6 K/min between 10 and 25 min after start up. The heating rate then decreased steadily to less than 1 K/min at about 35 min after start up. The initial heating rate lags only slightly behind the heating rate for the alumina plasma sprayed portion of the cathode, indicating the conduction from the higher temperature alumina

plasma sprayed portion to the steel portion. Interestingly, the heating rate stabilized during the same 10 to 25 min time frame as the anode cone and axial support bar, rather than continuing to decrease. This may be further indication of interaction between the cathode and xenon as discussed earlier. Figure 27 shows the heating rate for the alumina plasma sprayed portion of the cathode, which was SP04 in Figure 21.

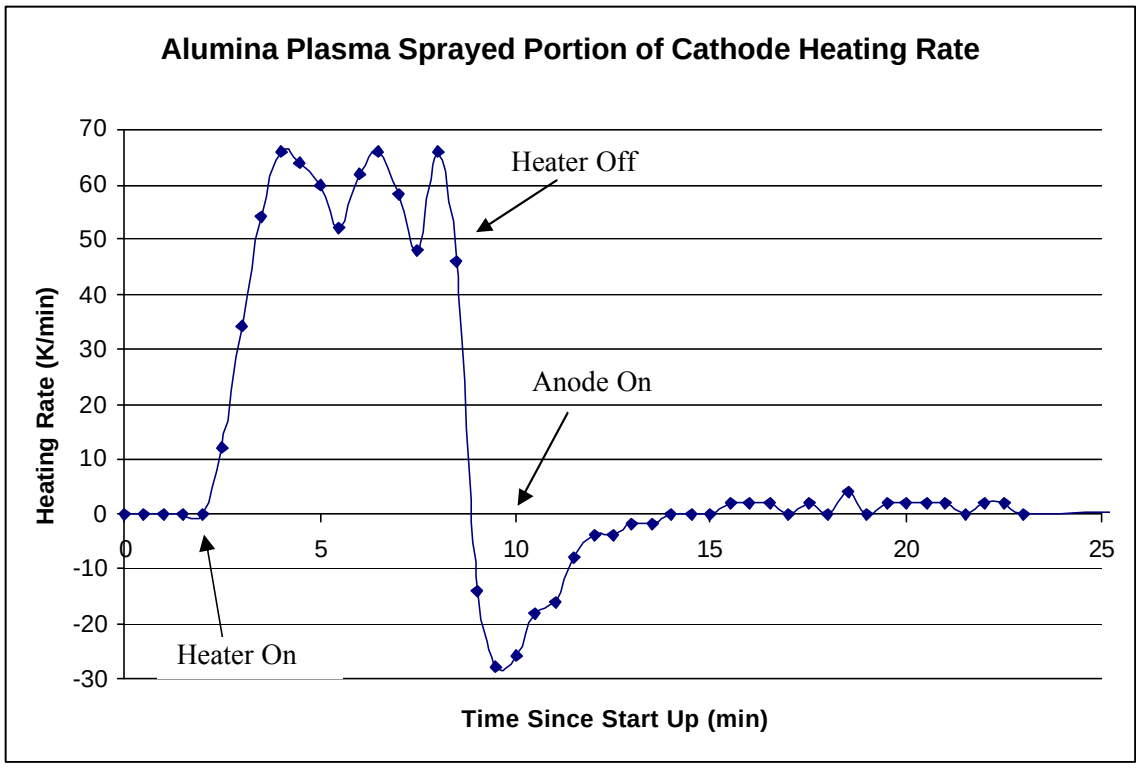

Figure 27: Alumina Plasma Sprayed Portion of the Cathode Heating Rate

The cathode was conditioned and at a temperature of 353 K at the zero time point. The heating rate increased rapidly over a span of 2 min to 60 K/min and remained between 50 and 70 K/min until the 9 min mark. The heating rate then reached negative values until the 13 minute mark. This variation is likely due to keeper heating during the first 10 minutes, followed by cathode flow start. The inverse relationship between cathode flow and keeper temperature caused the cathode heating rate to reach negative values. The heating rate is less than 1 K/min beginning with the 13 min mark.

Figure 28 shows Figure 25, Figure 26, and Figure 27 on one chart in order to further show the relation between the timing of the heating rates of the various components.

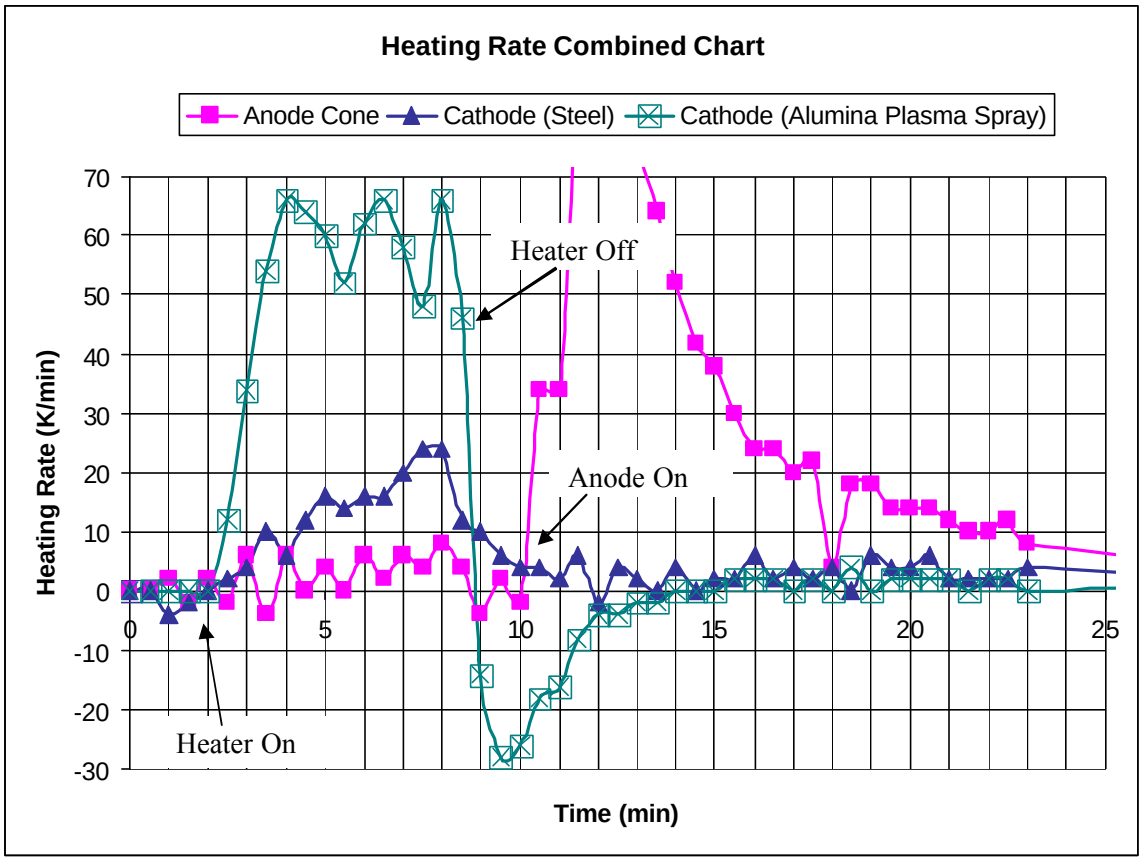

Figure 28: Component heating rates in single chart

As expected, the heating rate of the steel part of the cathode follows the heating rate of the alumina plasma sprayed part of the cathode due to conduction. However, as the anode heating rate increased, the heating rate of the steel part of the cathode stabilized instead of continuing to decrease as expected to follow the heating rate of the alumina plasma sprayed part of the cathode. Since the anode and the cathode are not connected, and the heating rate of the anode increased when xenon flow was initiated, the heating

rate of the steel part of the cathode may be due to interaction with the xenon, as suggested earlier.

Steady state results taken from thruster side view image

Once the temperature of the thruster components had reached a steady state, a single ThermaCam Researcher Image, file tc0501.fff, was analyzed for steady state temperature values. Although the anode cone was corrected for an emissivity of 0.45, the temperatures were still above the 773 K camera limit. Similarly, when an emissivity of 0.23 was applied to account for the alumina plasma sprayed portion of the cathode, the temperatures for the area were above 773 K. Unfortunately, since the actual temperature is unknown, this does not directly yield the hollow cathode insert temperature, which is a factor affecting cathode life. Since the anode cone and alumina plasma sprayed portions seen in the image were above the 773 K camera limit, the ThermaCam Researcher image in Figure 29 is shown with the object emissivity set to 0.20 for the steel portions of the thruster.

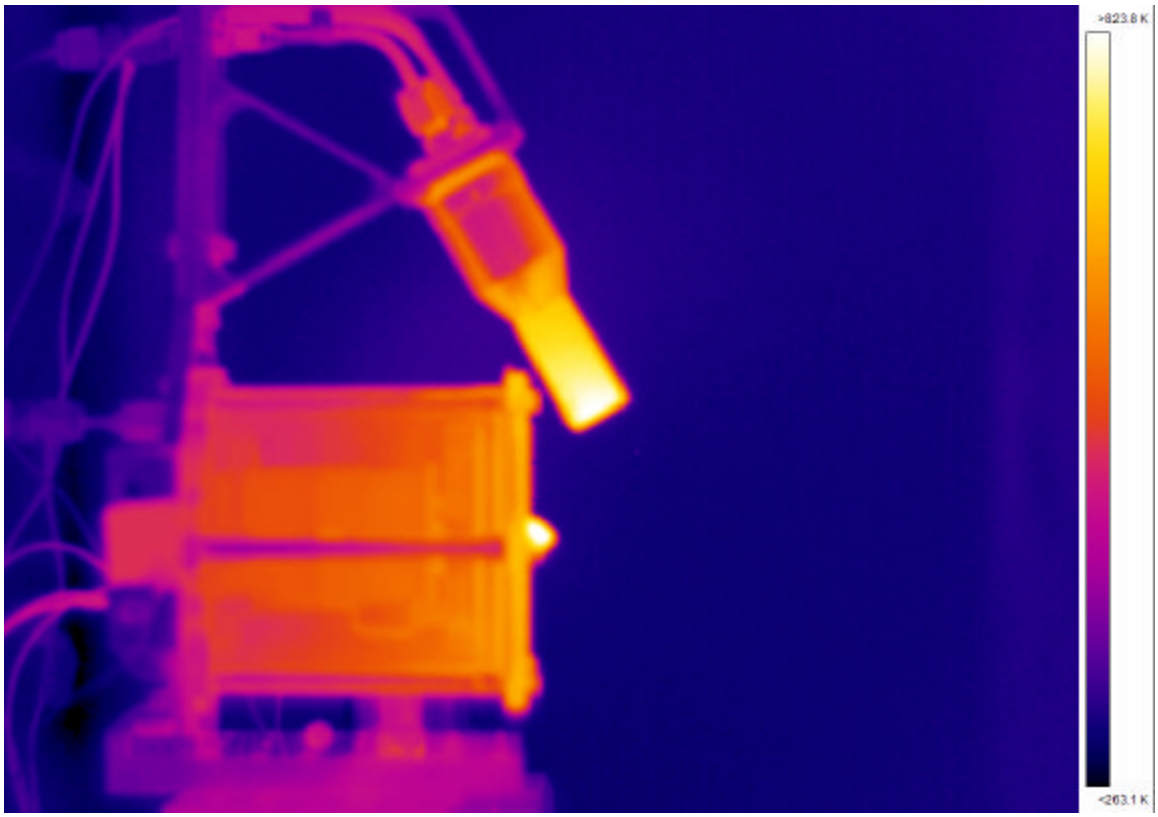

Figure 29: Side View Steady State Temperature Image

Temperatures on the upper constant diameter steel portion of the cathode are approximately 473 K near the center and 600 K near the edge. The increase in temperature at the edges is due to metals exhibiting an increase in emissivity, and therefore temperature, at high angles of emission as shown in Figure 30 (4:119) for titanium.

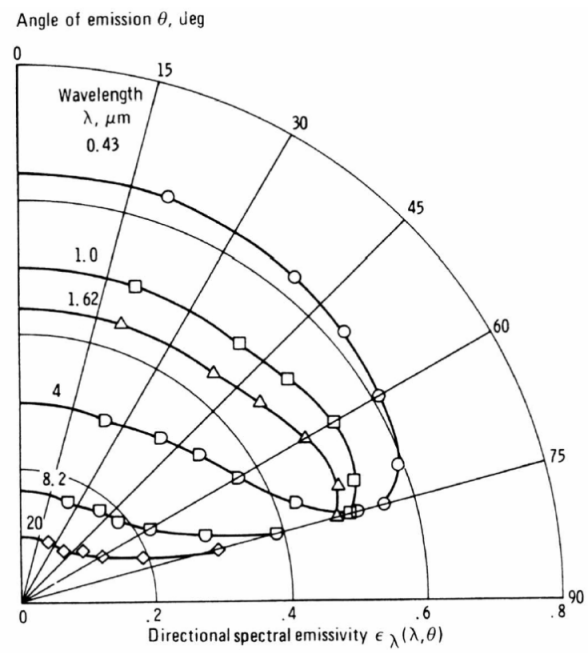

Figure 30: Emissivity and angle of emission (14:119)

The data for a wavelength of 8.2 μm falls within the wavelength range of 7.5 μm to 13 μm detected by the camera. The area of the cathode that decreases in diameter as it nears the alumina plasma sprayed portion of the cathode had temperatures ranging from 563 K to above 773 K. These temperatures are higher than the constant diameter steel section of the cathode, and may also be due to reflections or interaction with the xenon as it moved away from the exit plane and was obstructed by the cathode and thruster body. This is also evident in other images discussed later. The axial support bars decrease in temperature from 500 K near the exit plane to 420 K near the rear of the thruster. The magnet core windings can also be seen in the image, even though the core is physically inside the wire mesh of the thruster body. The core temperatures range from 620 K near the exit plane to 475 K near the rear of the thruster. While these temperatures represent the magnet core windings, supposing the magnet core is near this temperature suggests that it is not near the Curie temperature for iron of 1043 K or the Curie temperature of

858 K of iron alloyed with nickel. Still, reducing the temperature of the magnet core or using a material with a higher Curie temperature may increase the magnetic field strength and therefore increase the efficiency of the thruster.

Cooling rate results taken from thruster side view images

The next set of data shows the cooling rates during the 5 hours following thruster shut down from operation at 8.5 sccm. For reference, the spot locations are identical to those used to collect heating rate data as shown in Figure 21. Figure 31 shows the cooling rate data for the axial support bar near the exit plane, which is spot SP01 on Figure 21.

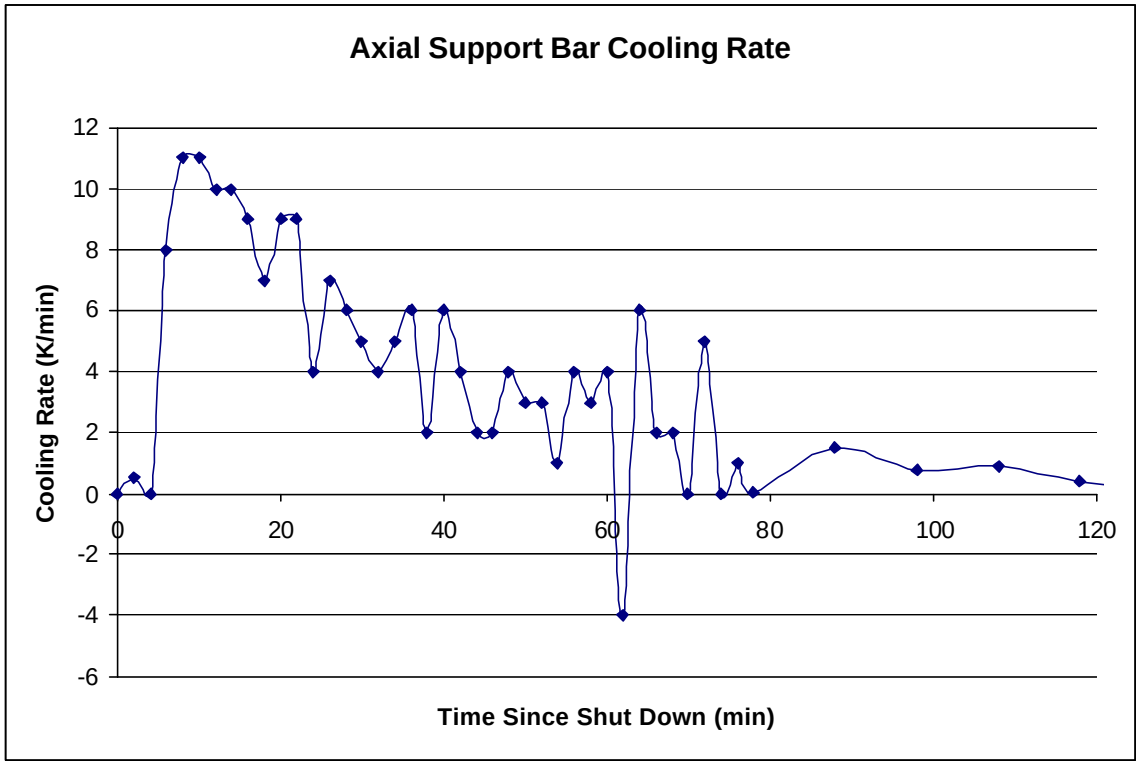

Figure 31: Axial Support Bar Cooling Rate

The initial cooling rate is 10 K/min and gradually decreases to less than one K/min at a time of 98 min after shut down. Compared to the other areas of the thruster analyzed for cooling rate, this cooling rate is relatively low due a lower emissivity and the lower

temperature difference between the axial support bar and the surroundings. Figure 24 shows the cooling rate for the anode cone, which is spot SP02 in Figure 21.

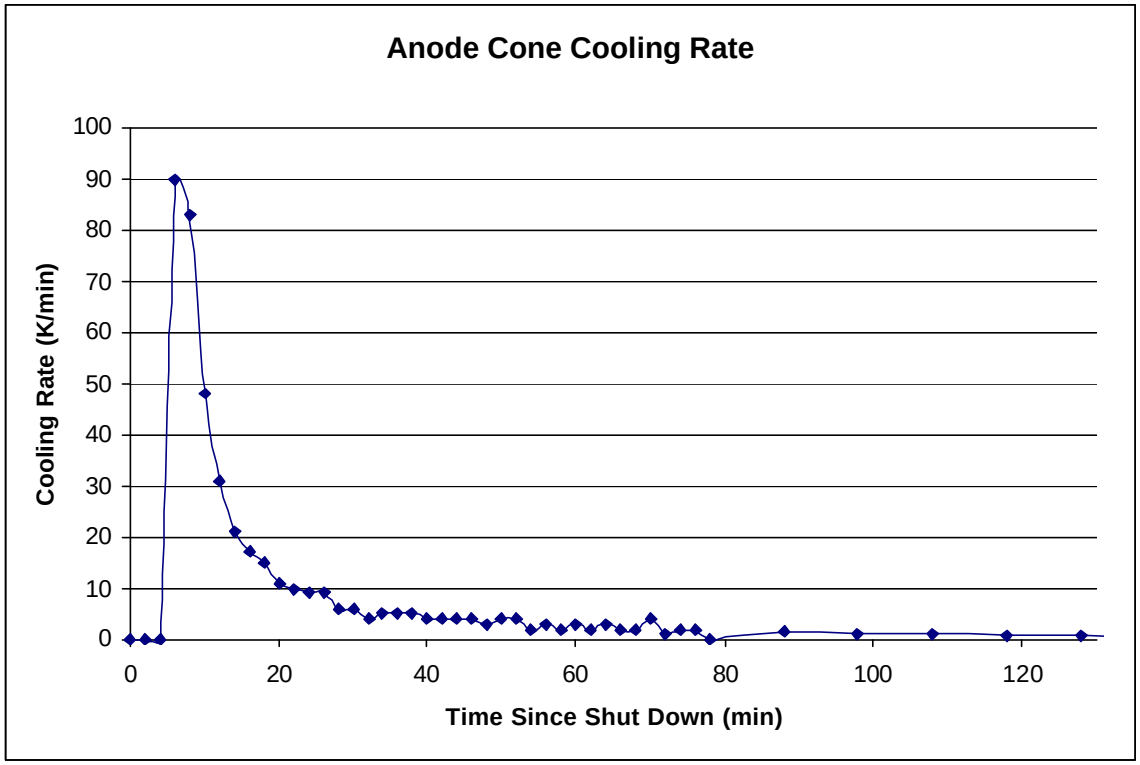

Figure 32: Anode Cone Cooling Rate

The anode cone shows an initial cooling rate of 90 K/min with a gradual decrease to less than 1 K/min at a time of 118 min after shut down. Compared to the other areas of the thruster analyzed for cooling rate, this cooling rate is the highest due a high emissivity and the higher temperature difference between the anode cone and the surroundings. Figure 33 shows the cooling rate for the steel portion of the cathode, which is spot SP03 in Figure 21.

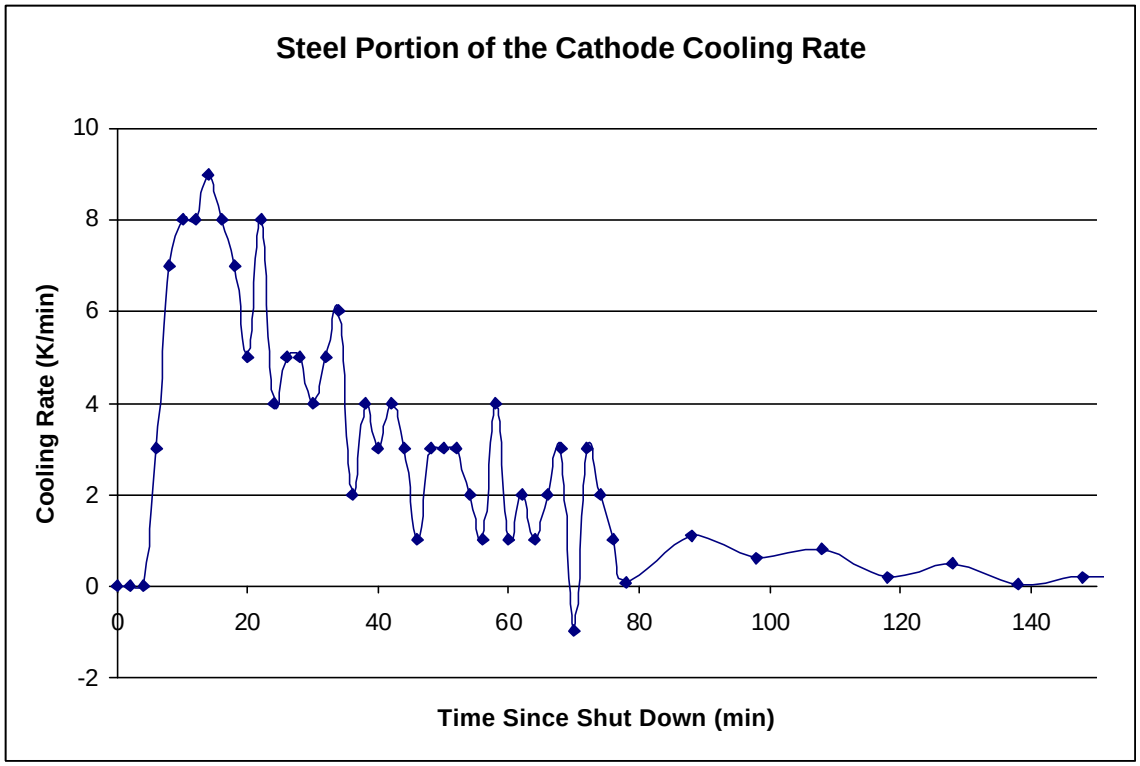

Figure 33: Steel Portion of the Cathode Cooling Rate

The steel portion of the cathode shows an initial cooling rate of 8.0 K/min with a gradual decrease to less than one K/min at a time of 98 min after shut down. Compared to the other areas of the thruster analyzed for cooling rate, this cooling rate is about the same as the axial support bar with the same emissivity and similar temperature difference between the steel and the surroundings. Figure 34 shows the cooling rate for the alumina plasma sprayed portion of the cathode, which was spot SP04 in Figure 21.

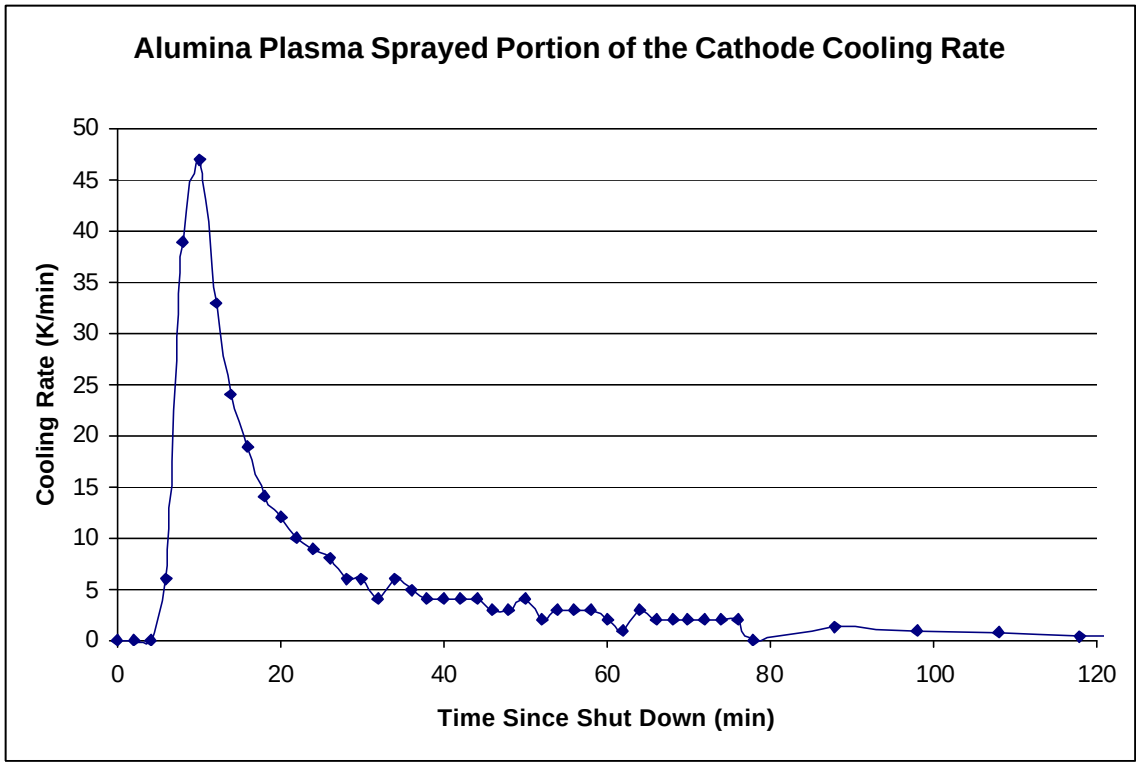

Figure 34: Alumina Plasma Sprayed Portion of the Cathode Cooling Rate

The alumina plasma sprayed portion of the cathode shows an initial cooling rate of nearly 50 K/min with a gradual decrease to less than one K/min at a time of 108 min after shut down. Compared to the other areas of the thruster analyzed for cooling rate, this cooling rate is relatively high due to the higher temperature difference between the alumina plasma sprayed portion of the cathode and the surroundings.

Temperature results with exit plane facing camera

The image from ThermaCam Researcher shown in Figure 35 shows the exit plane at a 45° angle to the camera.

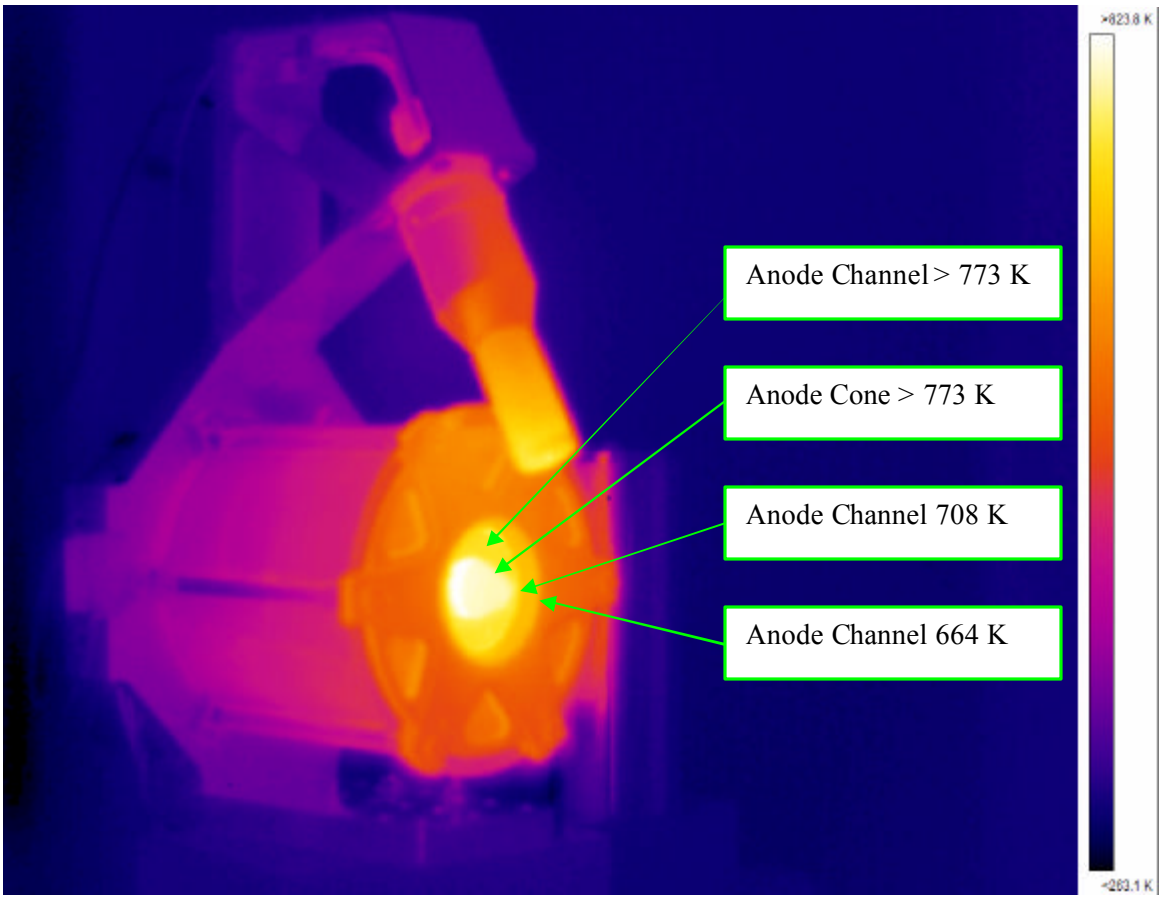

Figure 35: ThermaCam Researcher Image of Thruster at 45° Angle to Camera

The emissivity for the entire image was set to 0.45 for the boron nitride anode cone and anode channel since these are the areas of interest for this image. Unfortunately, the temperatures of the anode cone and the majority of the anode channel appear to exceed the capability of the camera to read temperatures over 773 K. The material in this section of the anode channel appears different from the material of a small ring near the exit plane (see Figure 6). The small ring within the anode channel nearest the exit plane is not above 773 K, and the temperatures there range from 664 K to 708 K as shown in the figure. It is interesting to note the temperature pattern on the upper steel portion of the cathode shown in Figure 36 with the 45 degree view on the left and the side view on the right.

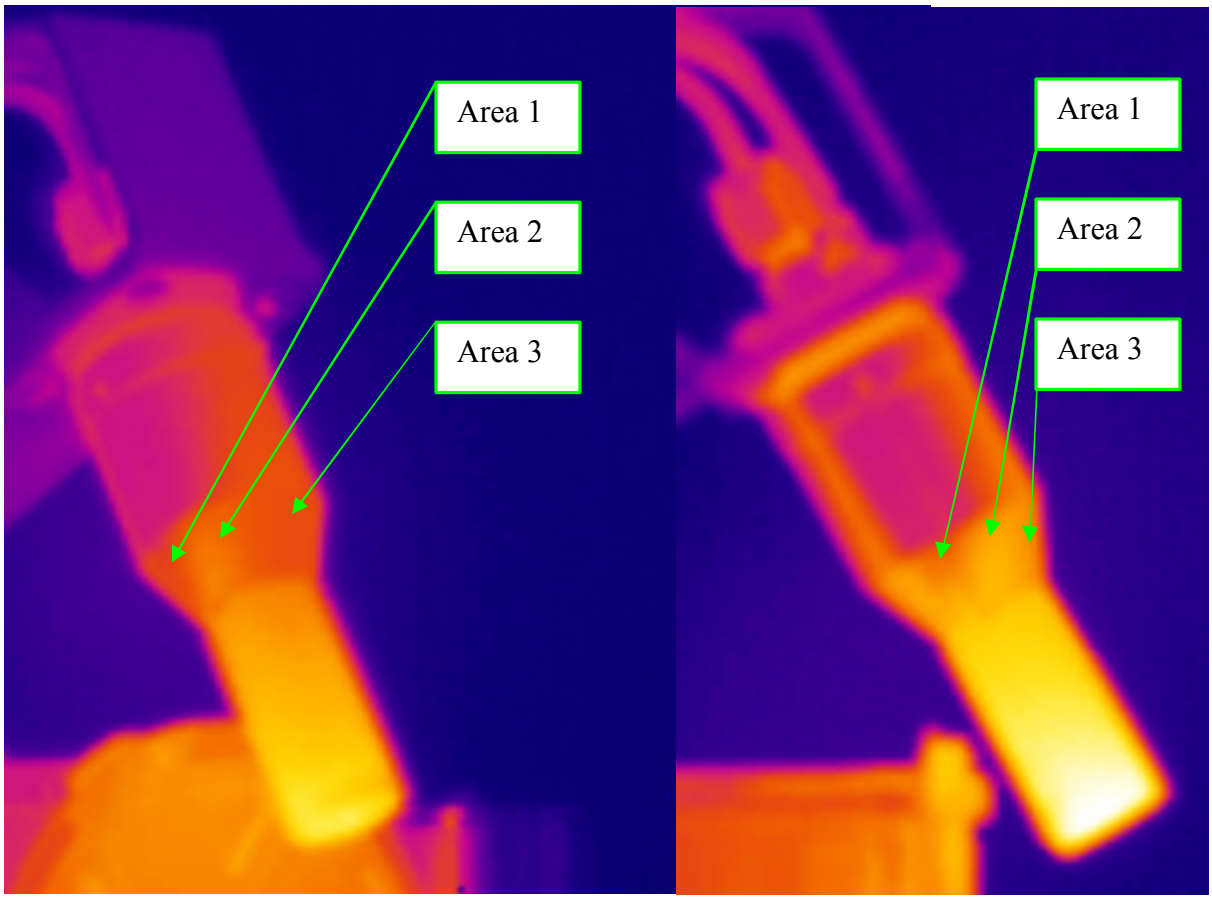

Figure 36: Temperature Pattern on Upper Steel Portion of the Cathode

If the xenon neutral interaction suggested earlier is feasible, the pattern might be explained by a flow field of the xenon around the cathode. The xenon flow may come up from the anode channel area and be blocked by the thruster body or have a free path to the upper portion of the cathode causing the different temperature in area 1 and area 2 respectively as shown in the figure. The lower temperature in area 3 may be due to partial flow blockage by the alumina plasma sprayed portion of the cathode. Accurate determination of the flow patterns in this area is complicated and beyond the scope of this work, but may be beneficial as a future project. While the actual temperatures in the upper steel portion of the cathode are not as critical as others, determining that the flow

patters found match the flow patterns observed here may further add weight to the idea of xenon neutral flow in this area.

The surface plot of the temperatures for the composite image with the thruster exit plane facing the camera is shown in Figure 37.

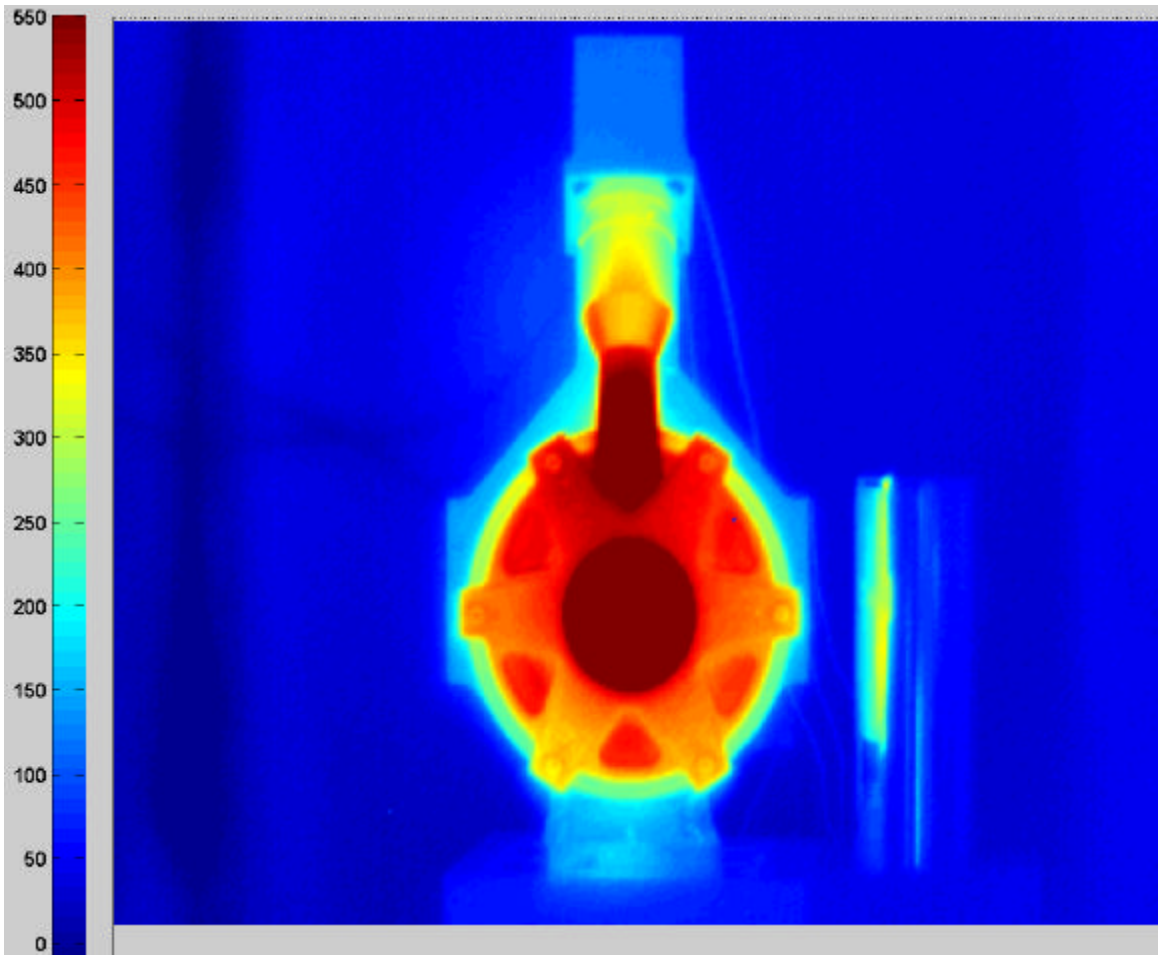

Figure 37: Surface Plot of Temperatures with Exit Plane Facing Camera

Temperatures of the alumina plasma sprayed portion of the cathode and the anode area shown in dark red exceed the 773 K limit capability of the camera. The upper steel portion of the cathode ranges in temperature of 725 K near the alumina plasma sprayed portion to a temperature of 575 K near the cathode mount. In addition, the steel portion of the cathode decreasing in diameter as it nears the alumina plasma sprayed portion of the cathode shows the sides are hotter than the center, while the constant diameter

portions of the steel cathode show the opposite. As discussed earlier, this may be due to reflections not accounted for in the analysis or due to interaction with the xenon as it moves away from the exit plane. A ThermaCam image with emissivity set to 0.23 is shown in Figure 38 for a visual comparison.

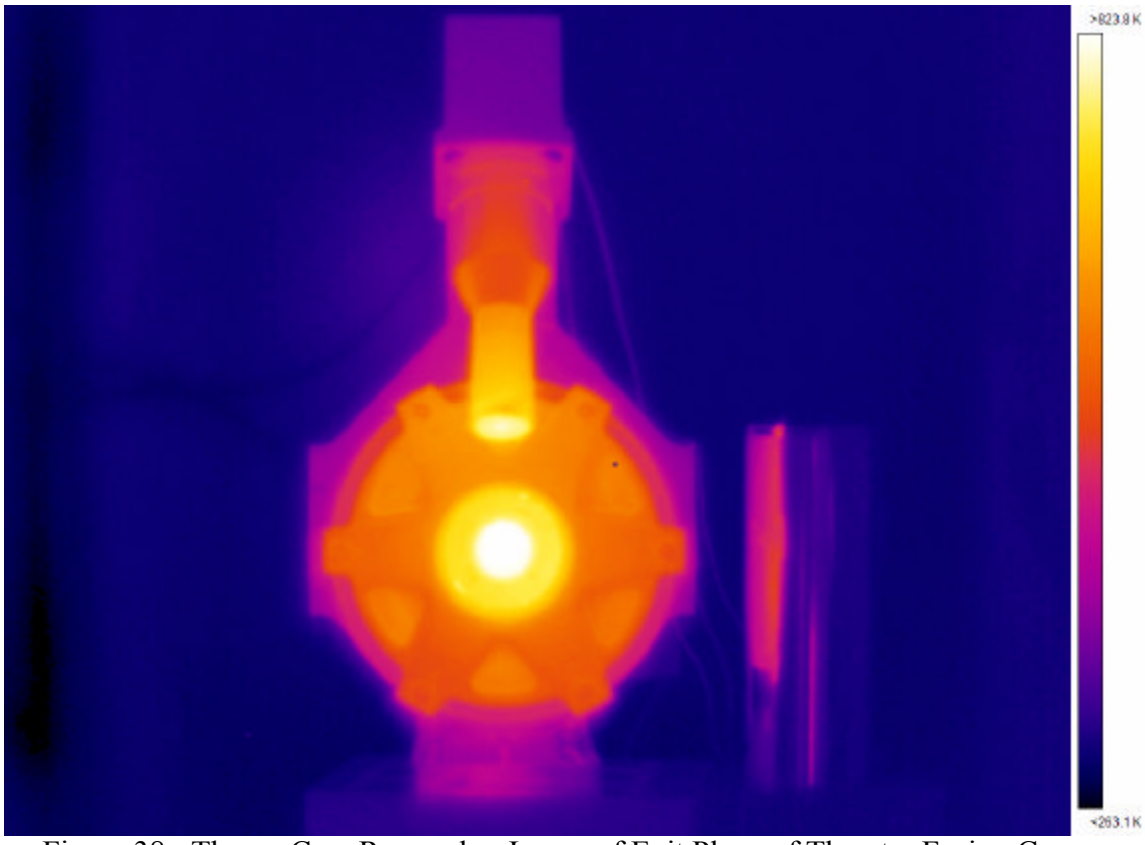

Figure 38: ThermaCam Researcher Image of Exit Plane of Thruster Facing Camera

The small dark spot in the upper right quadrant of the alumina plasma sprayed portion of the exit plane is a camera anomaly, not an actual spot on the thruster.

Cooling rate results taken from images with thruster exit plane facing camera

The cooling rate data included here originates in the ThermaCam Researcher data files from tc1220.fff to tc3349.fff. The cooling rate for the anode cone is shown in Figure 39, which is SP01 from Figure 22.

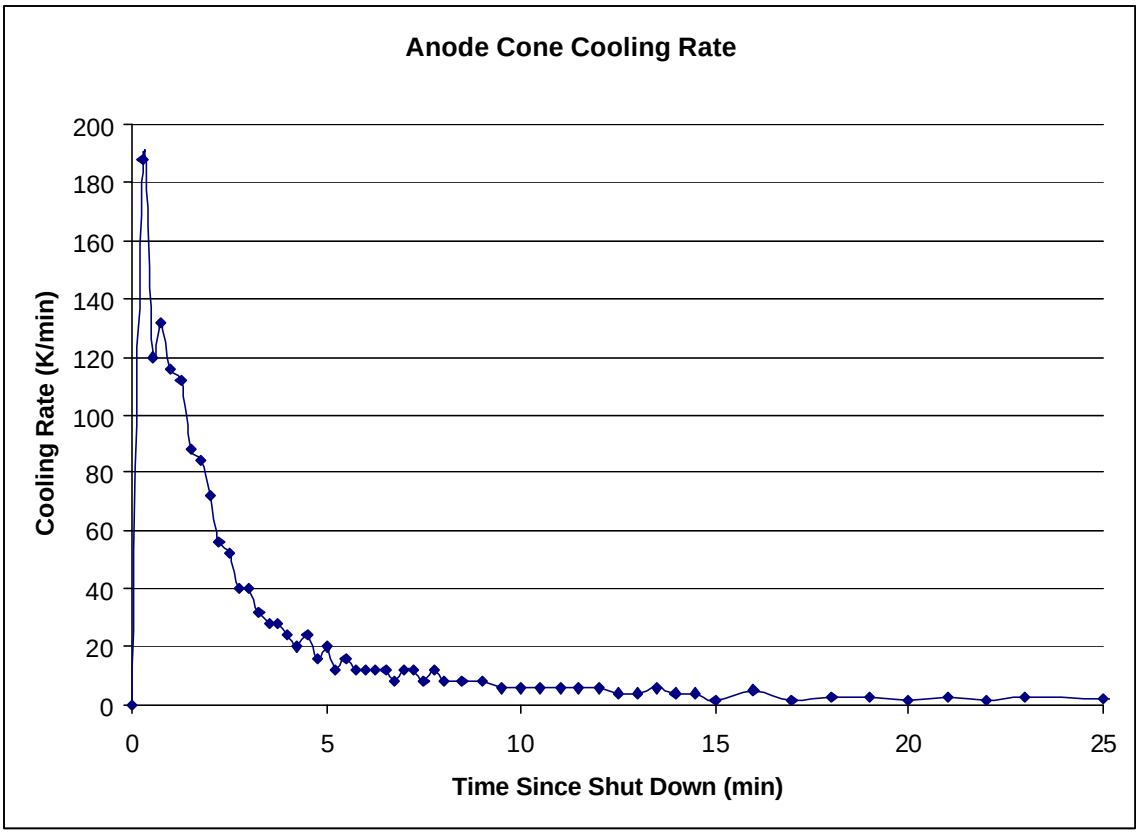

Figure 39: Exit Plane Anode Cone Cooling Rate

The cooling rate was between 188 K/min and 112 K/min in the first two minutes. The cooling rate of the anode cone taken from the side view data was not taken from the exact same spot on the cone and was only 90 K/min suggesting this area of the anode cone was hotter. The cooling rate gradually decreased to about 20 K/min and then remained less than 3 K/min at the 23 min mark. The cooling rate for the rear of the anode channel is shown in Figure 40, which was SP02 in Figure 22.

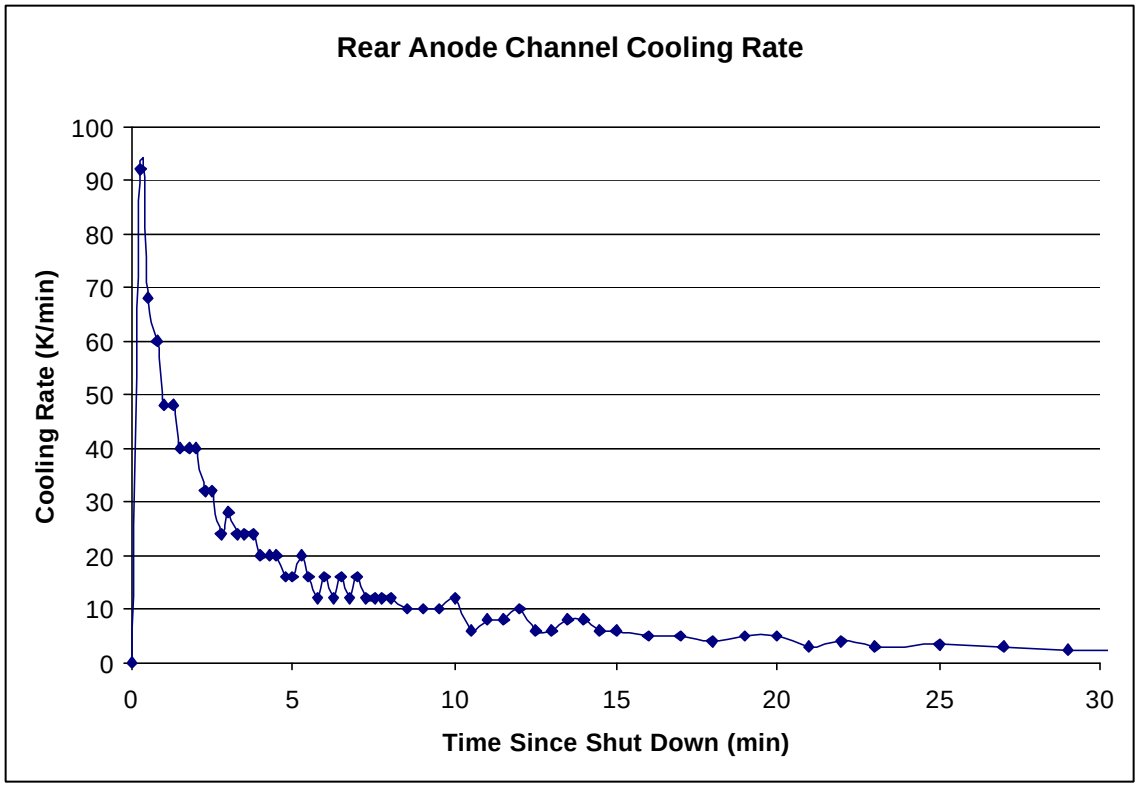

Figure 40: Rear Anode Channel Cooling Rate

The cooling rate began at 92 K/min and fell rapidly to about 14 K/min in the first eight minutes. This cooling rate is lower than the cooling rate of the anode cone, suggesting the anode cone was at a higher temperature. The cooling rate gradually decreased to about 20 K/min and then remained less than 3 K/min at the 27 min mark. The cooling rate data for the rear of the alumina plasma sprayed portion of the exit plane is shown in Figure 41, which was SP03 in Figure 22.

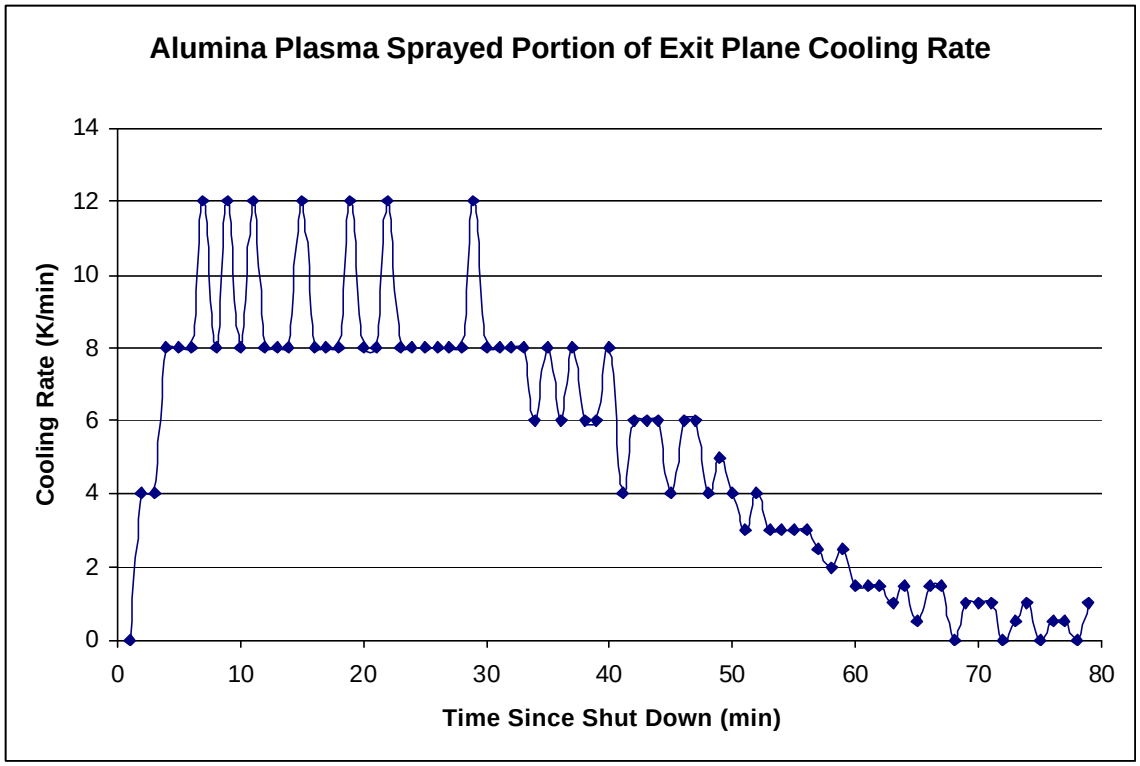

Figure 41: Alumina Plasma Sprayed Portion of Exit Plane Cooling Rate

The cooling rate appears to vary between 8 K/min and 12 K/min during the first 30 minutes of observation. The apparent variation in cooling rate during this period is due to the change in temperature of only 2 K during one 15 second period to 3 K during the next 15 second period, and back to 2 K during the next 15 second period. Therefore, due to the small temperature changes, it is more accurate to view the cooling rate as 10 K/min. Afterward, the cooling rate decreased steadily to less than 3 K/min at the 56 min mark. The cooling rate data for the cathode tip is shown in Figure 42, which was SP02 in Figure 22.

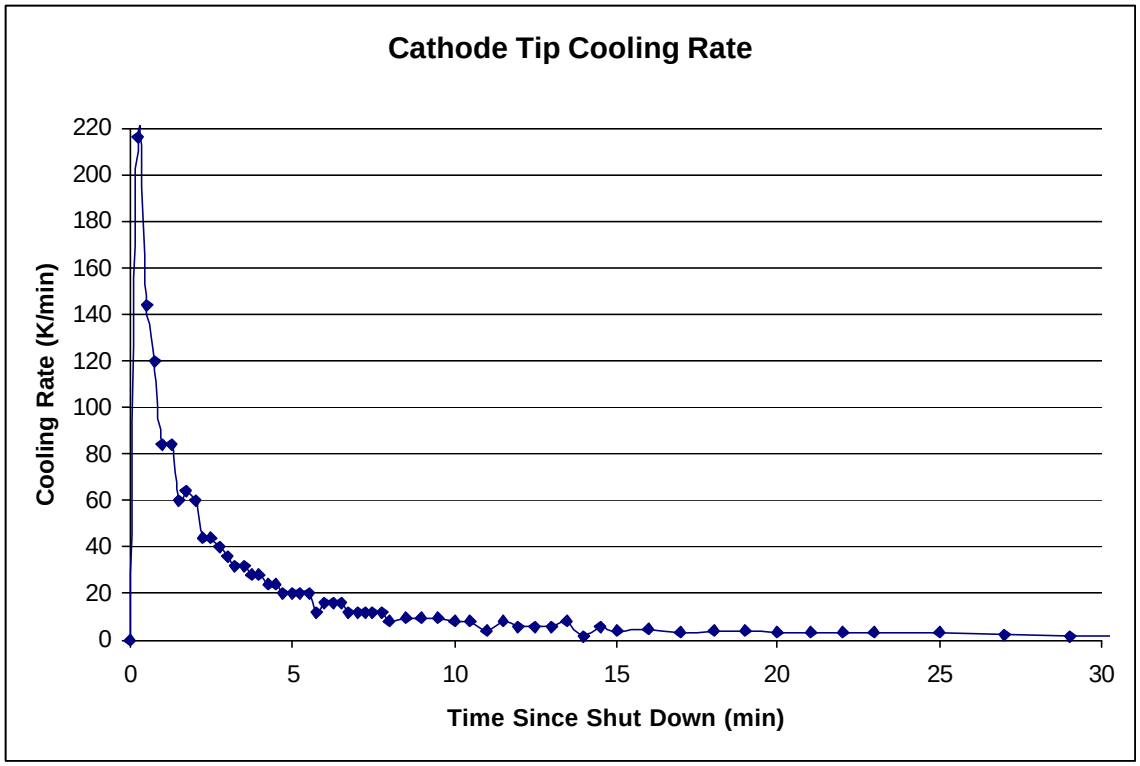

Figure 42: Cathode Tip Cooling Rate

The cooling rate began at 218 K/min then rapidly decreased to 20 K/min. The cathode tip is likely the hottest area on the thruster and thus had the highest cooling rate. The cooling rate was less than 3 K/min at the 25 min mark.

V. Conclusions and Recommendations

Conclusions

Temperature is an important factor impacting thruster design and lifetime, so it is beneficial to obtain temperature data. The temperature data for this work was gathered using a thermal imaging camera and a zinc selenide window as a non-intrusive means to view an operating Hall thruster inside a vacuum chamber. The following discussion reveals conclusions concerning the benefits and difficulty of using a thermal imager including knowledge of the actual emissivity, the temperature of the magnet as it relates to thruster efficiency and lifetime, and the possibility of xenon interaction with the thruster components.

The benefits of using thermal imaging are: it does not require modification of the thruster, does not require vacuum chamber opening and closing to correct any imaging problems, and it provides temperature data over the entire visible surface of the thruster. There are drawbacks to thermal imaging, such as the complexity of correcting the raw temperature data to a more correct temperature, camera temperature limitations, and an increased cost of operating a thermal imaging system over the use of conventional means, such as thermocouples. Values such as object emissivity, distance between the object and the camera, optics temperature and transmissivity, atmospheric temperature and humidity, and reflected temperature can be entered directly into the camera software to correct the image. The largest difficulty of using a thermal imager comes from the need to know specific emissivity values for the actual object components and accounting for the different emissivity values to create a single image with corrected temperatures. While some values can be obtained from reference material, these values may not be

accurate if the material has undergone any changes since being manufactured, as was the case for this experiment. In addition, obtaining emissivity values by adjusting the camera input emissivity value was possible for the steel parts of the thruster, but this method is not always practical due to the very high temperatures of the parts as compared to the capability of the thermocouples and additionally, in the case of the anode cone, the location within the plasma. The impact of emissivity ambiguity on measured temperature caused a worst-case variation of ± 48 K for the steel, ± 63 K for the boron nitride, and ± 92 K for the alumina plasma spray. With steel temperature reaching the 500 K range, and the boron nitride and alumina plasma sprayed parts of the thruster potentially above 700 K these values represent a 8 % to 12 % error in values. These benefits and limitations must be kept in mind when considering the use of thermal imaging.

Heating rate and cooling rate values were obtained for the axial support bars, the steel and alumina plasma sprayed portions of the cathode, and the anode cone. The heating rate for the axial support bars and steel portion of the cathode were less than 20 K/min while the alumina plasma sprayed portion of the cathode experienced a heating rate between 60 K/min and 70 K/min and the anode cone saw the largest peak heating rate of 136 K/min. The heating rate for all the parts was less than 5 K/min within 30 min after thruster start up. The cooling rate of the axial support bar and the steel portion of the cathode were less than 12 K/min while the alumina plasma sprayed portion of the cathode experienced an initial peak cooling rate of 47 K/min and the anode cone saw initial peak cooling rate of 90 K/min. These heating and cooling rates are indicative of the operating conditions experienced by the thruster following a start up and shut down. A comparison of the heating rate data of the individual components suggested possible

interaction of the xenon with the thruster components. It is also possible the steady state data supports this idea, but there was no direct indication of the interaction.

Steady state temperatures on the alumina plasma sprayed portion of the cathode and on the anode cone and anode channel walls exceeded the 773 K limit of the thermal imager since filters were not used to increase the maximum temperature to the actual limit of 2275 K. While knowing these temperatures exceed 773 K is useful, it would be more helpful if the actual temperatures were known. The ability to learn the actual temperatures also depends on knowing the actual emissivity of the alumina plasma sprayed portion of the cathode and the anode cone and channel walls, as discussed earlier. The magnet core winding temperatures range from 620 K near the exit plane to 475 K near the rear of the thruster. While these temperatures represent the magnet core windings, supposing the magnet core is near this temperature suggests it is not near the Curie temperature for iron of 1043 K or the Curie temperature of 858 K of iron alloyed with nickel. Still, reducing the temperature of the magnet core or using a material with a higher Curie temperature may increase the magnetic field strength and therefore increase the efficiency of the thruster.

Recommendations for Future Research

Since the emissivity of the various parts of the thruster differs from reference values, and it has been shown that the largest temperature error resulted from uncertainty of the exact value, it is recommended the actual emissivity values be obtained experimentally. If possible, artificial heating of the components and comparison of thermocouple temperatures to those obtained with a thermal imager with the emissivity value varied until the temperatures are the same would increase accuracy. This would

allow for future temperature monitoring on the thruster and enable the data in this work to be revised with the new emissivity values in order to obtain more accurate results, as long as the revised temperatures fall below the maximum temperature limit of the camera. The data taken during the thruster start up at 7 sccm followed by steady state at 7 sccm and a flow increase to 10 sccm followed by thruster rotation should also be analyzed with the revised emissivity values. If this is not possible due to inability to raise the component temperature to a level near operating temperature or at least show that the emissivity is no longer changing with increasing temperature, an alternate method of cleaning the thruster before testing to remove the discolored film could restore the emissivity to a value closer to reference values. For example, removing the film on the steel mount of the thruster was easily done by using very light pressure on a wire brush after the experiment. While this is not as desirable as obtaining the actual emissivity by experiment, it is better than leaving the thruster as it is.

Future experiments using thermal imaging should include the use of filters to allow the camera to display temperatures above 773 K. This was a limiting factor for determining the temperature of the alumina plasma sprayed portion of the cathode and the anode cone and channel walls if the emissivity values were correct.

The view factor between thruster components and between the thruster and the vacuum chamber components was not determined. Finding the view factor using computer modeling would further increase the accuracy of the temperature data.

Appendix A – Data Collection Experimental Log

Data was collected on September 26-27, 2006 and included thruster operation during start up, shut down, steady state conditions as follows in the following sections. The ThermaCam Researcher software captures each frame of temperature data naming the file appropriately for experiment start/event/stop times, and is placed after the clock time for reference purposes

Thruster start up to 8.5 sccm followed by shut down and 5 hour cool down

On the first day, the thruster position, side view with the exit plane facing to the right, allowed data capture during start up to steady state, then to capture the cool down after the thruster shut down with little plume interference. The thruster cathode was conditioned, taking three hours and is required any time the thruster has been exposed to atmosphere. The thruster start-up procedure achieved a flow of 85%, which is 8.5 standard cubic centimeters per minute (sccm). At 1234 hrs (tc0137.fff), the data capture rate on ThermaCam Researcher was set to capture one frame every 30 sec. The thermocouples were set to record temperature every second. The thruster operated until the temperature measured at several points on the thruster appeared to reach steady state. Steady state was one-degree temperature change in 30 minutes. At 1620 hrs (tc0586.fff), the thruster was shutdown and data collection was continued at a rate of one frame per minute for five hours until 2122 (tc0886.fff) in order to capture cooling rate data.

Thruster start-up to 8.5 sccm, 90° rotation, and cool down

On the second day of testing, the ThermaCam Researcher data capture rate was set to one frame per two seconds and the thruster was started at 0804 hrs to a flow rate

8.5 sccm. At 0830 hrs, the thruster was rotated at 15° increments such that the exit plane rotated from its normal right facing position to a position where the exit plane was directly facing the camera. At 0834 hrs, the thruster was shut down and data was recorded until 0948 hrs.

Thruster startup to 7.0 sccm and steady state

At 0958 hrs, the ThermaCam Researcher data capture rate was set to one frame per 30 seconds beginning with frame tc4083.fff, and the thruster started to flow at 7.0 sccm. At 1245 hrs, it was noted researcher software indicated "no connection" with camera. The fire wire connection between the camera and the computer was checked, but there were no problems with the connection. Next, it was attempted to reconnect using the ThermaCam Researcher software, but a "device not present" error was received. Since the computer did not seem to be malfunctioning, the fire wire connection was disconnected and reconnected and a second attempt to reconnect using researcher software was made, but again the "device not present" error was received. It appeared the ThermaCam Researcher software was functional, but it would not connect with the camera. As a result, data after 1113 hrs was lost. The computer was rebooted, and upon start up of the ThermaCam Researcher software, the camera was recognized and showed as "connected". Since a different computer recorded the thermocouple data, there was no thermocouple data lost. It appeared the temperature of the thruster had reached steady state by 1245 hrs according to a visual inspection of the data for thermocouple #2. At 1304 hrs, with the ThermaCam Researcher data capture rate remaining at one frame per 30 seconds, data was collected with the thruster at steady state at 7.0 sccm until 1330 hrs.

Thruster flow increase from 7.0 sccm to 10.0 sccm

At 1331 hrs, the flow rate was increased from 7.0 sccm to 10.0 sccm, and the thruster was allowed to operate until 1607 hrs. The variation in flow rate was meant to capture thruster temperatures while at the low and high end of thruster operation.

Thruster rotation and shutdown

At 1610 hrs, the ThermaCam Researcher data capture rate was set to one frame per sec and thruster was rotated at 15° increments such that the exit plane rotated from its normal right facing position to a position where the exit plane was directly facing the camera. The thruster was shut down at 1611 hrs.

Thruster cool-down with exit plane facing camera

After the thruster shutdown as 1611 hrs, with the exit plane of the thruster facing the camera, the ThermaCam Researcher data capture rate was set to one frame per minute. The thruster cooled down until 1729 hrs. At 1732 hrs, the chamber coolers stopped to allow the chamber to pressurize slowly, to prevent moisture formation on the coolers. Data was still recorded for four hours during the pressurization process. The chamber was not fully pressurized and opened until the following day at 1039 hrs.

Appendix B – Tabular Data Used for Error Analysis

Table 13: Steel Temperature Error Due to Emissivity

Steel	Spot Location in ThermaCam Researcher X = 70, Y = 161	
Emissivity	**Temperature (K)**	**Delta T (K)**
0.1	495	23
0.12	472	18
0.14	454	14
0.16	440	12
0.18	428	9
0.2	419	9
0.22	410	7
0.24	403	6
0.26	397	5
0.28	392	5
0.3	387	NA

Table 14: Boron Nitride Temperature Error Due to Emissivity

Boron Nitride	Spot Location in ThermaCam Researcher X = 161, Y = 157	
Emissivity	**Temperature (K)**	**Delta T (K)**
0.37	812	17
0.39	795	15
0.41	780	14
0.43	766	14
0.45	752	12
0.47	740	12
0.49	728	10
0.51	718	11
0.53	707	NA

Table 15: Alumina Plasma Spray Temperature Error Due to Emissivity

Alumina Plasma Spray	Spot Location in ThermaCam Researcher X = 169, Y = 105	
Emissivity	**Temperature (K)**	**Delta T (K)**
0.15	764	35
0.17	729	30
0.19	699	25
0.21	674	21
0.23	653	19
0.25	634	16
0.27	618	14
0.29	604	13
0.31	591	NA

Table 16: Air Transmissivity Temperature Error

Input Humidity (%)	Input Temperature (C)	Calculated Transmissivity	Calculated Temperature (K)
20	297	1.00	419
30	297	1.00	419
40	297	0.99	419
50	297	0.99	419
60	297	0.99	419
70	297	0.99	419
50	278	1.00	419
50	288	1.00	419
50	293	0.99	419
50	297	0.99	419
50	303	0.99	419
50	308	0.99	419
50	317	0.99	419

Table 17: Window Transmissivity Temperature Error

Window Transmissivity (%)	Calculated Temperature (K)	Delta T (K)
0.58	424	1
0.59	423	2
0.60	421	1
0.61	420	1
0.62	419	2
0.63	417	1
0.64	416	1
0.65	415	1
0.66	414	NA

Table 18: Distance Temperature Error

Distance (m)	Calculated Temperature (K)
0.50	419
0.55	419
0.60	419
0.65	419
0.72	419
0.80	419
1.00	419
2.00	419
4.00	419
5.00	420

Table 19: Reflected Temperature and Temperature Error

Reflected Temperature (K)	Calculated Temperature (K)	Delta T (K)
283	430	2
285	428	3
287	425	3
289	422	3
291	419	3
293	416	4
295	412	3
297	409	4
299	405	NA

Bibliography

1. "Hall Effect Thruster.", n. pag. http://en.wikipedia.org/wiki/Hall_effect_thruster , April, 2006

2. Humble, Ronald W., et al, "*Space Propulsion Analysis and Design*", The McGraw-Hill Companies, Inc., 1995

3. Larson, Wiley J. and Wertz, James R., *Space Mission Analysis and Design*, 3nd ed., Microcosm Press, El Segundo, California, 2005

4. Hargus, William A., "A Diagnostic for Hall Thruster boron nitride Insulator Erosion", Air Force Research Lab, Edwards AFB, CA, 2004

5. Low Power Nominal Specifications, Busek Co. Inc., 2005

6. High Power Nominal Specifications, Busek Co. Inc., 2005

7. Liu, Shiquan, et al, "Magnetism of Iron Containing MCM-41 Spheres", Journal of Magnetism and Magnetic Materials, 280 (2004) 31-36

8. "Curie Point", n. pag. http://en.wikipedia.org/wiki/Curie_point, January, 2007

9. "Thermionic emission", n. pag. http://en.wikipedia.org/wiki/Thermionic_emission , August, 2006.

10. "Hollow Cathodes", n. pag. http://www.engr.colostate.edu/ionstand/research_hollowcathodes.html , August, 2006

11. Van Nord, J., Kamhawi, H., McEwen, H.K., "Characterization of a High Current, Long Life Hollow Cathode" NASA TM-214095, 2006

12. Sarver-Verhey, Timothy R., "Scenario for Hollow Cathode End-of-Life", NASA/CR-2000-209420

13. Yim, John T. et. al, "An Investigation of Factors Involved in Hall Thruster Wall Erosion Modeling", AIAA-2006-4657

14. Siegel, Robert and Howell, John R., *Thermal Radiation Heat Transfer*, 4th ed, Taylor & Francis, New York, New York, 2002, Chapter 4.

15. ThermaCam Researcher Users' Manual, FLIR Systems, Pub No. 1558071, Rev A52, Issued June 7, 2004

16. Incropera, Frank P., DeWitt, David P., *Fundamentals of Heat and Mass Transfer*, 5th ed, John Wiley & Sons, Hoboken, NJ, 2002

17. Thermoanalytics, n. pag, http://www.thermoanalytics.com/support/faq/answers/tracer.html , December, 2006

18. CFD Flow Modeling, n. pag, http://www.fluent.com/software/fluent/heat.htm , December, 2006

19. Rees, W. G., *Physical Principles of Remote Sensing*, 2nd ed., Cambridge University Press, The Edinburgh Building, Cambridge CB2 2RU, UK, 2005

20. Thermovision A40M Operator's Manual, FLIR Systems, Pub No. 1557813, Rev A72, Issued Oct 29, 2004

21. Crofton, M.W. et al., "Calibrated Infrared Imaging for Electric Thrusters", AIAA-1996-2977

22. Infrared Training Center, n. pag. http://www.infraredtraining.com/gallery/ir_image_list/application_id/1000/, June 2006

23. Infrared Thermography for Predictive Maintenance, FLIR Systems, I030100AR

24. Cooper, Rob, "Thermography Inspection at Poplar Creek Power Station, Fort McMurray, AB", April 24, 2006

25. Hargus, William A., "Laser Induced Fluorescence of Neutral Xenon in the Near Field of a 200 W Hall Thruster", AIAA-2005-4400

REPORT DOCUMENTATION PAGE

Form Approved
OMB No. 074-0188

The public reporting burden for this collection of information is estimated to average 1 hour per response, including the time for reviewing instructions, searching existing data sources, gathering and maintaining the data needed, and completing and reviewing the collection of information. Send comments regarding this burden estimate or any other aspect of the collection of information, including suggestions for reducing this burden to Department of Defense, Washington Headquarters Services, Directorate for Information Operations and Reports (0704-0188), 1215 Jefferson Davis Highway, Suite 1204, Arlington, VA 22202-4302. Respondents should be aware that notwithstanding any other provision of law, no person shall be subject to an penalty for failing to comply with a collection of information if it does not display a currently valid OMB control number.
PLEASE DO NOT RETURN YOUR FORM TO THE ABOVE ADDRESS.

1. REPORT DATE *(DD-MM-YYYY)*	2. REPORT TYPE	3. DATES COVERED *(From – To)*
22 Mar 2007	**Master's Thesis**	August 2005 – March 2007

4. TITLE AND SUBTITLE
Characterization of a Hall Effect Thruster Using Thermal Imaging

5a. CONTRACT NUMBER

5b. GRANT NUMBER

5c. PROGRAM ELEMENT NUMBER

6. AUTHOR(S)

Tomaszewski, James William, Capt, USAF

5d. PROJECT NUMBER

5e. TASK NUMBER

5f. WORK UNIT NUMBER

7. PERFORMING ORGANIZATION NAMES(S) AND ADDRESS(S)
Air Force Institute of Technology
Graduate School of Engineering and Management (AFIT/EN)
2950 Hobson Way, Building 640
WPAFB OH 45433-8865

8. PERFORMING ORGANIZATION REPORT NUMBER
AFIT/GA/ENY/07-M18

9. SPONSORING/MONITORING AGENCY NAME(S) AND ADDRESS(ES)
Air Force Research Lab / Space Propulsion Branch
Attn: Mr. Michael Huggins
5 Pollux Drive
Edwards Air Force Base, CA, 93524

10. SPONSOR/MONITOR'S ACRONYM(S)
AFRL/PRS

11. SPONSOR/MONITOR'S REPORT NUMBER(S)

12. DISTRIBUTION/AVAILABILITY STATEMENT

APPROVED FOR PUBLIC RELEASE; DISTRIBUTION UNLIMITED.

13. SUPPLEMENTARY NOTES

14. ABSTRACT

A Hall thruster uses ionized xenon as a propellant for space propulsion applications. The heat produced by thruster components and the xenon plasma transfers to space and the spacecraft, impacting thruster and spacecraft design, as well as thruster efficiency and lifetime. Therefore, thermal information was gathered and analyzed in order to better understand the thermal characteristics of an operating thruster and to provide data applicable to improving the thruster efficiency and lifetime. This paper contains analysis of thruster temperatures obtained using a commercially available FLIR A40M thermographic imager in order to characterize a Busek Inc. 200W Hall Effect Thruster operating in Chamber 6 at the Air Force Research Laboratory at Edwards AFB, CA. This method is non-intrusive in that the thruster is viewed from outside the chamber through a zinc selenide window and provides temperature data on the entire visible area of the thruster for output to a computer for further processing. Maximum temperatures observed were above 773 K on the alumina plasma sprayed portion of the cathode, the anode, and on the thruster body near the exit plane. Magnet core winding temperature varied from 620 K near the exit plane to 475 K near the rear of the thruster. If these temperatures are near the magnet core temperature, it suggests they are not near the Curie temperature for iron of 1043 K or the Curie temperature of 858 K of iron alloyed with nickel. Initial heating rates of up to 138 K/min and initial cooling rates of up to 218 K/min were observed. The steady state temperature images and the heating data indicated a possible interaction between xenon and the thruster components.

15. SUBJECT TERMS
Hall, Thermal, Imaging, Thruster, Xenon, Propulsion, Zinc, Selenide, Emissivity, Transmissivity

16. SECURITY CLASSIFICATION OF:			17. LIMITATION OF ABSTRACT	18. NUMBER OF PAGES	19a. NAME OF RESPONSIBLE PERSON
a. REPORT	b. ABSTRACT	c. THIS PAGE			Richard D. Branam, Maj, USAF
U	U	U	UU	86	19b. TELEPHONE NUMBER *(Include area code)* (937) 785-3636, ext 7485; e-mail: (Richard.Branam@afit.edu)

Standard Form 298 (Rev. 8-98)
Prescribed by ANSI Std. Z39-18